Sulfur_X: A model of sulfur degassing during magma ascent

Shuo Ding[1], Terry Plank[1], Paul J. Wallace[2], Daniel J. Rasmussen[3]
[1] Lamont Doherty Earth Observatory, Columbia University, NY
[2] Department of Earth Sciences, University of Oregon, OR
[3]Mineral Sciences, National Museum of Natural History, Smithsonian, Washington, D.C.

Corresponding author: Shuo Ding (sd3210@columbia.edu)

This paper is a non-peer review preprint submitted to EarthArXiv. This paper has been submitted to *Geochemistry, Geophysics, Geosystems* for peer review.

Key Points:

- Sulfur_X is a new, open source magma degassing model that accurately predicts the volatile and redox evolution of ascending arc magmas.
- Sulfur_X shows that sulfur can start degassing in the lower crust or near-surface, depending on the initial $S^{6+}/\Sigma S$ and H_2O in the melt.
- The vapor compositions predicted by Sulfur_X can be used to interpret the CO_2/S_T ratios in high-*T* volcanic gases, an eruption precursor.

Abstract

The degassing of CO_2 and S from arc volcanoes is fundamentally important to global climate, eruption forecasting, ore deposits, and the cycling of volatiles through subduction zones. However, all existing thermodynamic/empirical models have difficulties reproducing CO_2-H_2O-S trends observed in melt inclusions and provide widely conflicting results regarding the relationships between pressure and CO_2/SO_2 in the vapor. In this study, we develop an open-source degassing model, Sulfur_X, to track the evolution of S, CO_2, H_2O, and redox states in melt and vapor in ascending mafic-intermediate magma. Sulfur_X describes sulfur degassing by combining separate sulfur partition coefficients for three equilibria: RxnI. FeS (m) + H_2O (v)→H_2S (v) + FeO (m), RxnIa. FeS (m) + 1.5O_2 (v) →SO_2 (v) +FeO (m), and RxnII. $CaSO_4$(m)→SO_2 (v) + O_2 (v) + CaO (m), based on the sulfur speciation in the melt (m) and co-existing vapor (v). Sulfur_X is also the first to track the evolution of fO_2 and sulfur and iron redox states accurately in the system using electron balance and equilibrium calculations. Our results show that a typical H_2O-rich (4.5 wt.%) arc magma with high initial $S^{6+}/\Sigma S$ ratio (>0.5) will degas much more (~2/3) of its initial sulfur at high pressures (> 200 MPa) than H_2O-poor ocean island basalts with low initial $S^{6+}/\Sigma S$ ratio (<0.1), which will degas very little sulfur until shallow pressures (<50 MPa). This new pressure-S relationship in the melt predicted by Sulfur_X provides new insights into interpreting the CO_2/S_T ratio measured in high-T volcanic gases in the run-up to eruption.

Plain Language Summary

Understanding the process by which CO_2 and S are emitted from volcanoes, called degassing, is important in interpreting the CO_2/S_T gas precursors to volcanic eruptions and quantifying the total amount of climatically important gases released to the atmosphere. However, existing models show significant discrepancies in predicting the behavior of sulfur during degassing. In this study, we employ a new approach to describe sulfur behavior during magma degassing and develop a new model, Sulfur_X, that successfully reproduces the distinct S, CO_2, and H_2O records from different volcanoes. Sulfur_X shows that sulfur can either degas early at high pressure or late at low pressure during magma ascent to the surface, depending on the initial sulfur speciation and H_2O contents in the magma. In addition, sulfur is one of the most commonly measured volcanic gas components for volcano monitoring. Therefore, the predicted compositional evolution of co-existing vapor by Sulfur_X during magma decompression bears directly on the interpretation of CO_2/S_T ratio measured in high-T volcanic gases and the development of eruption forecasts models.

1. INTRODUCTION

Degassing of arc magmas is the dominant modern mechanism through which volatiles (H_2O, C, S, and halogens) stored inside the Earth enter the surface environment, with significant effects on climate and redox evolution. Geochemical quantification of gas emissions is also becoming increasingly critical to understanding how volcanoes prepare to erupt. Given that sulfur can be present in both oxidized and reduced form in melt and vapor, degassing of sulfur during magma ascent has been invoked as the primary mechanism that drives redox changes in basaltic magmas (Moussallam et al., 2016; Brounce et al., 2017; Longpré et al., 2017). Currently, three approaches, including volcanic gas observations, microanalysis of volatiles in mineral-hosted melt inclusions, and thermodynamic modeling, are commonly used to investigate volcanic degassing. In particular, models of volcanic degassing can link the geochemical records of volcanic gases and melt inclusions (e.g., Werner et al., 2020). Thus, the three approaches studied in concert provide the most powerful approach to understanding volcanic degassing.

Modeling equilibrium degassing of CO_2 and S is commonly employed to understand the CO_2/SO_2 ratio in volcanic gases, CO_2 and S contents in mineral-hosted melt inclusions, and degassing depths (Scaillet and Pichavant, 2003; Burton et al., 2007). For example, a sudden increase in the CO_2/SO_2 ratio in high temperature volcanic gases has been observed prior to eruptions in several arc volcanoes worldwide (Werner et al., 2019) and the anomaly has been modeled as a surge of deeply sourced CO_2-rich gas, based on the contrasting pressure effects on the solubility of CO_2 and S from existing models (Burton et al., 2007; Aiuppa et al., 2016; J.M. de Moor et al., 2016). This interpretation is supported by results of modeling volatile evolution in melt inclusions that complement volcanic gas (Scaillet and Pichavant, 2003). Melt inclusions captured inside crystals at varying depths have the potential to record the magma degassing path as a function of pressure and initial composition. However, post-entrapment processes can modify melt inclusion compositions (Anderson and Brown, 1993; Danyushevsky *et al.*, 2000; Gaetani *et al.*, 2012; Métrich and Wallace, 2008; Moore *et al.*, 2015). Notably, recent developments in thermodynamic modeling (Steele-Macinnis et al., 2011; Wallace et al., 2015; Rasmussen et al., 2017; Steele-MacInnis et al., 2017; Moore et al., 2018), Raman spectroscopy (Esposito et al., 2012; Hartley et al., 2014; Moore et al., 2015; Aster et al., 2016) and experimental rehomogenization (Mironov et al., 2015; Moore et al., 2018; Rasmussen et al., 2020) have reconstituted the CO_2 concentration in melt and demonstrated that vapor bubbles present inside melt inclusions can host up to 90% of the CO_2 in the bulk inclusion. Figure 1 shows the CO_2 and S concentration from experimentally rehomogenized melt inclusions from Volcán de Fuego in Guatemala (Rasmussen et al., 2020). Compared to naturally quenched Fuego melt inclusions (Lloyd et al., 2013), the maximum CO_2 content in the rehomogenized inclusions increases by 400% (Fig. 1). Although S concentration in the melt inclusions was not changed by rehomogenization, S decreases with decreasing CO_2 along the reconstituted degassing trend, which differs dramatically in shape and magnitude from the untreated melt inclusions.

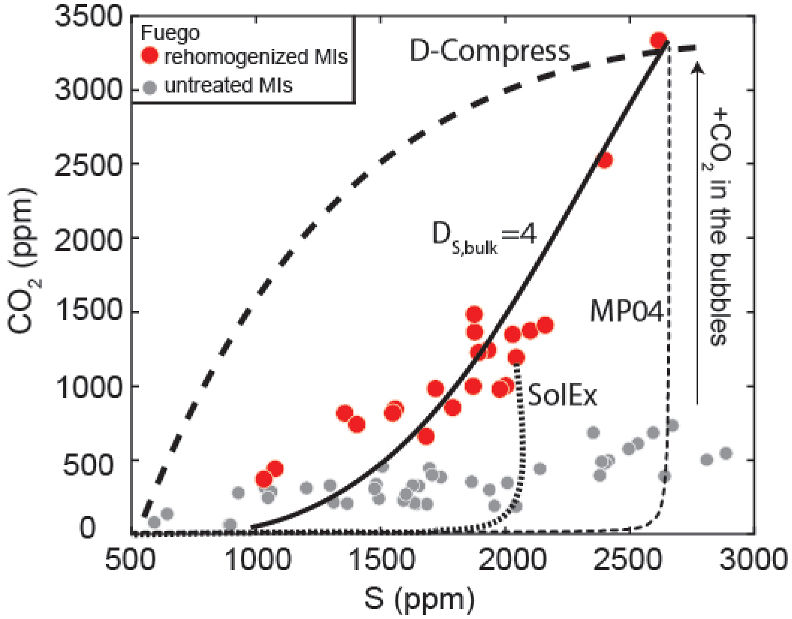

Figure 1. Comparisons of CO_2 and S concentration in experimentally rehomogenized (red circles, Rasmussen et al., 2020) and untreated (grey circles, Lloyd et al., 2013) melt inclusions from Fuego (Guatemala) volcanoes with modeled degassing trends from D-Compress (Burgisser et al., 2015), SolEx (Witham et al., 2012), MP04 (Moretti and Papale, 2004), and an empirical model (R2020) with a constant bulk partition coefficient $(D_S^{non-melt/melt} = 4)$ for sulfur (Rasmussen et al., 2020). All forward models show significant mismatch with the rehomogenized melt inclusion data. The empirical fit, D-Compress and MP04 all start with 4.5 wt.% H_2O, 3300 ppm CO_2, and ~2600 ppm S. SolEx is forced to start at 400 MPa, the highest pressure can be applied in the model, with 4.3 wt.% H2O, ~1100 ppm CO_2 and 2100 ppm S.

The S-CO_2 co-degassing trend revealed by the rehomogenized melt inclusions from Fuego (as well as Seguam volcano) by Rasmussen et al. (2020) challenges the conventional understanding that S only degasses at low pressure, after CO_2 is almost entirely degassed from the ascending magma (Webster and Botcharnikov, 2011; Lesne et al., 2011; Witham et al., 2012) and calls into question the interpretation that the increase of CO_2/S in volcanic gas results from an influx of deep, CO_2-rich magma. None of the existing forward degassing models can reproduce the CO_2-S co-variation shown in Figure 1. Moreover, different degassing models predict contrasting CO_2-S degassing paths (Figure 1) with similar initial conditions. All these forward models are based on parameters relating the S concentration or fugacity in the gas and the S concentration in the silicate melt, such as sulfide/sulfate solubilities (Burgisser et al., 2015), sulfide/sulfate capacities (Scaillet and Pichavant, 2003; Moretti and Papale, 2004), and sulfur partition coefficients (Witham et al., 2012). However, none of these parameters were well calibrated by xperiments at pressures higher than 300 MPa (O'Neill and Mavrogenes, 2002; Moune et al., 2008; Lesne et al., 2011; Zajacz et al., 2012; Zajacz et al., 2013; Fiege et al., 2014b; Zajacz, 2014; Beermann et al., 2015; Fiege et al., 2015; Masotta et al., 2016; Nash et al., 2019; Gennaro et al., 2020), which might have led to inaccurate extrapolation at high pressures. Furthermore, some of the existing experiments could suffer from the formation of sulfide solids (Masotta et al., 2016; Gennaro et al., 2020), inaccurate estimate of fO_2 (Lesne et al., 2011; Fiege et al., 2014b; Fiege et al., 2015), S loss to the capsule (Lesne et al., 2011), which might have caused significant discrepancies among existing degassing models even at pressures of 300 MPa or lower.

Inspired by both the homogenized melt inclusion data and high-pressure experimental data, we develop a new degassing model as a Python program (available in GitHub:

https://github.com/sdecho/Sulfur_X.git), Sulfur_X, to predict the evolution of S, CO_2, and H_2O in basalt and basaltic andesite melts and co-existing vapor by combining existing COH degassing models (e.g., Iacono-Marziano et al., 2012; Newman and Lowenstern, 2002) with experimentally constrained gas-melt sulfur partition coefficients. This model also tracks redox evolution during closed-system S degassing by coupling S-Fe redox equilibrium in the melt with electron balance calculations as S species partition between melt and vapor.

2. BACKGROUND

2.1 Sulfur speciation in the melt and vapor

Sulfur is a multi-valent element. It exists primarily as $S^{2-}$and/or S^{6+} in basaltic melt (Jugo et al., 2010; Nash et al., 2019) and as SO_2 and/or H_2S in high-temperature vapor (Holloway, 1987, Figure 2a). The narrow fO_2 interval that marks the transition from $S^{2-}$to S^{6+} in basaltic melt (Fig. 2) overlaps with the oxygen fugacity range in arc magmas (Jugo et al., 2010). The dominant reaction of sulfur species in silicate melt can be written as follows.

$$S^{2-} + 8Fe^{3+} \rightarrow S^{6+} + 8Fe^{2+} \tag{1}$$

S speciation can be calculated as a function of $Fe^{3+}/\Sigma Fe$ in the melt and as a function of the equivalent fO_2 (Kress and Carmichael, 1991). Nash et al. (2019) derived the temperature dependence of this reaction by estimating its thermodynamic properties using solid analogs (e.g., FeS, $FeSO_4$, FeO, Fe_2O_3) and showed that it can successfully reproduce experimental results at different temperatures (Jugo et al., 2010; Botcharnikov et al., 2011a; Nash et al., 2019). However, it remains debatable whether solid analogs can be used to accurately model the temperature dependence of melt species, and whether the temperature dependence of this reaction in silicate melts is as large as estimated by Nash et al. (2019) (O'Neill, 2021; see also Wood et al., 2021). O'Neill's (2021) reassessment of Nash et al.'s thermodynamic modeling suggests a much small temperature dependence, and other experimental studies (Wilke et al., 2011; Matjuschkin et al., 2016, Beaudry and Grove, 2019) demonstrate that major-element composition, water content, and pressure could also all play a role in sulfur speciation in the melt. Muth and Wallace (2021) adopted O'Neill's smaller temperature dependence and proposed another $Fe^{3+}/\Sigma Fe$ and $S^{6+}/\Sigma S$ relation based on the Fe- and S- X-ray Absorption Near Edge Structure (XANES) spectroscopy data for olivine-hosted melt inclusions from the southern Cascade arc (Muth and Wallace, 2021).

Equilibrium between sulfur species in the vapor can be described as follows:

$$H_2S + \frac{3}{2}O_2 \rightarrow SO_2 + H_2O \tag{2}$$

Using the thermodynamic properties of the four involved gas components from NIST-JANAF Thermochemical Tables (DOI: 10.18434/T42S31 adopting a standard state of unit fugacity of the hypothetical ideal gas at a pressure of 1 atm and the temperature of interest for each component, the equilibrium constant of this reaction can be written as a function of temperature.

$$log_{10}(K_{SO2-H2S}(T)) = log_{10}\left(\frac{fSO_2 \times fH_2O}{fH_2S \times fO_2^{3/2}}\right) = 4.1245 - \frac{27110}{T(K)} \tag{3}$$

Therefore, the fSO_2/fH_2S ratio in the vapor can be calculated as a function of fO_2, fH_2O, and temperature. With knowledge of the fugacity coefficients of SO_2 and H_2S at a given pressure and temperature (Pingfang Shi and Saxena, 1992), fSO_2/fH_2S can be converted to the ratio of the mole fractions of SO_2 and H_2S.In our calculations, we have ignored minor S species such as S_2 and COS.

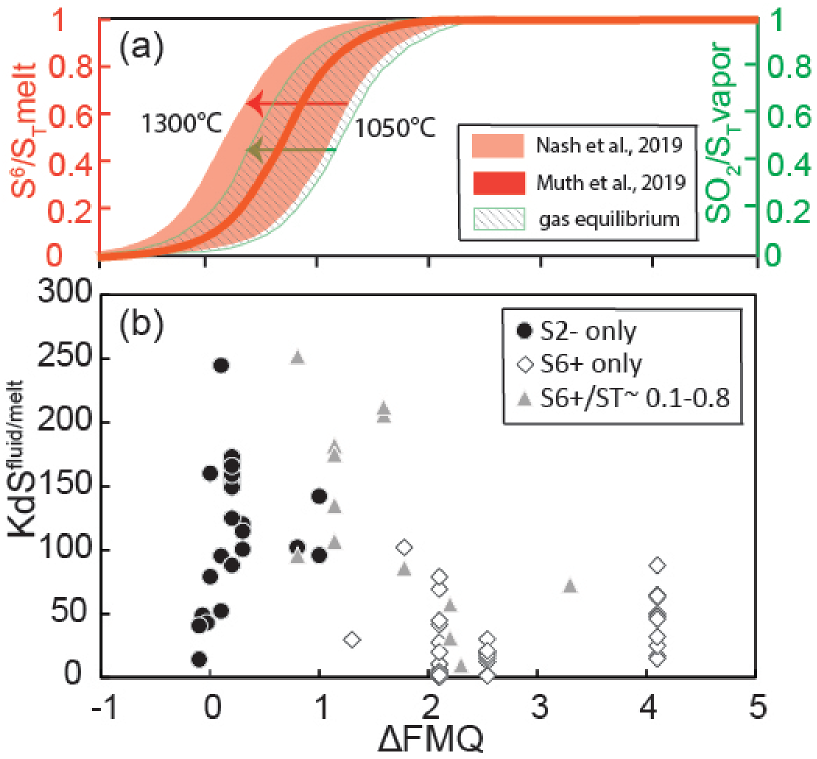

Figure 2. (a) Sulfur speciation in the melt (light and dark orange) and in the vapor (green) as a function of fO_2 calculated by (Nash et al., 2019), (Muth and Wallace, 2021) and the gas equilibrium equation 3. The fO_2 range where S^{2-} transitions to S^{6+} in the melt is predicted to shift one log10 unit lower by the Nash model when temperature increases from 1050 °C to 1300 °C (indicated by arrow in orange). In contrast, O'Neill's (2021) reassessment of Nash's thermodynamic model suggested only a very small temperature effect. Muth and Wallace (2021) adopted O'Neill's smaller temperature dependence and used Fe- and S-XANES data for hydrous arc melt inclusions to constrain the relationship shown by the dark orange curve (1300 °C at the left edge of the curve, to 1050 °C at the right edge). SO_2/S_T in the vapor phase also shifts by < one log10 unit when temperature increases from 1050 °C to 1300 °C (indicated by arrow in green). All the calculations are carried out at 200 MPa, with a basaltic melt composition and 60% H_2O in the vapor. (b) Experimentally determined partition coefficients ($kd_S^{v/m}$) of sulfur between fluid and basaltic-andesitic melt at pressure > 1atm (Moune et al., 2008; Lesne et al., 2011; Zajacz et al., 2012; Zajacz et al., 2013; Zajacz, 2014; Fiege et al., 2015; Masotta et al., 2016) as a function of fO2 (relative to the fayalite-magnetite-quartz buffer, ΔFMQ). The experiments are grouped into three categories based on the sulfur speciation in the melt: S^{2-} only (black circles), S^{6+} only (open diamonds), and a mixture of S^{2-} and S^{6+} (grey triangles). S speciation of each experiments is either that reported in the original experimental study, or calculated using the reported fO_2 (Kress and Carmichael, 1991; Nash et al., 2019).

2.2 Existing degassing models

Previous studies have established computational, thermodynamic models to predict the H_2O-CO_2-S evolution in magma and co-existing vapor as a function of *T*, *P*, melt composition, and

fO_2 (Table 1) and use the modeled results to interpret volcanic gas (Burton et al., 2007) and melt inclusion records (Scaillet and Pichavant, 2003). Figure 3 shows modeled degassing paths for H_2O, CO_2, and S in melt (Fig. 3a, b) and CO_2/SO_2 in co-existing vapor (Fig. 3c) calculated using SolEx (Witham et al., 2012), D-Compress (Burgisser et al., 2015) and the degassing model from Moretti and Papale (2004, refered as MP04) at conditions appropriate to Fuego. SolEx and MP04 show similar results for H_2O and CO_2 but are markedly different for S. D-Compress predicts different behavior for CO_2 and S compared to the other two forward models. More importantly, no existing forward models can reproduce the S-CO_2 evolution in melt revealed by the rehomogenized olivine-hosted melt inclusions from the Fuego 1974 eruption (Fig.1; Rasmussen et al., 2020). D-Compress predicts more rapid S degassing than CO_2 degassing in the melt (Fig.1b) with ~3300 ppm initial CO_2 and 2700 ppm initial S, and very low CO_2/SO_2 (<1) in the co-existing vapor along the entire degassing path (Fig. 3c). The predicted rapid S loss from the melt results from the unreasonably high total S contents (> 50 mol%) in the vapor at pressures higher than 300 MPa. D-Compress predicts high SO_2, H_2S and S_2 fugacity (discussed further in a later section), a result of the assumption that the system maintains vapor saturation with a given H_2O, CO_2 and total pressure without any input constraints for S (Burgisser et al., 2015). Moreover, the default S fugacity model employed by D-Compress is calibrated with sulfide/sulfate-saturated experiments at pressures ≤ 300 MPa (Moune et al., 2008; Beermann et al., 2011; Botcharnikov et al., 2011b). On the contrary, arc magma systems are not always saturated with sulfide minerals and are only rarely saturated with sulfate minerals or immiscible melts, and the actual degassing pressure could be greater than 300 MPa. Moretti and Papale (2004) and Scaillet and Pichavant (2003) employed the concept of sulfate and sulfide capacities to model sulfur behavior, and their models predict high CO_2/SO_2 (>15) in co-existing vapor until

very shallow depths (Fig. 3c). However, neither sulfate nor sulfide capacities are calibrated at pressures higher than 1 atm (O'Neill, 2021).

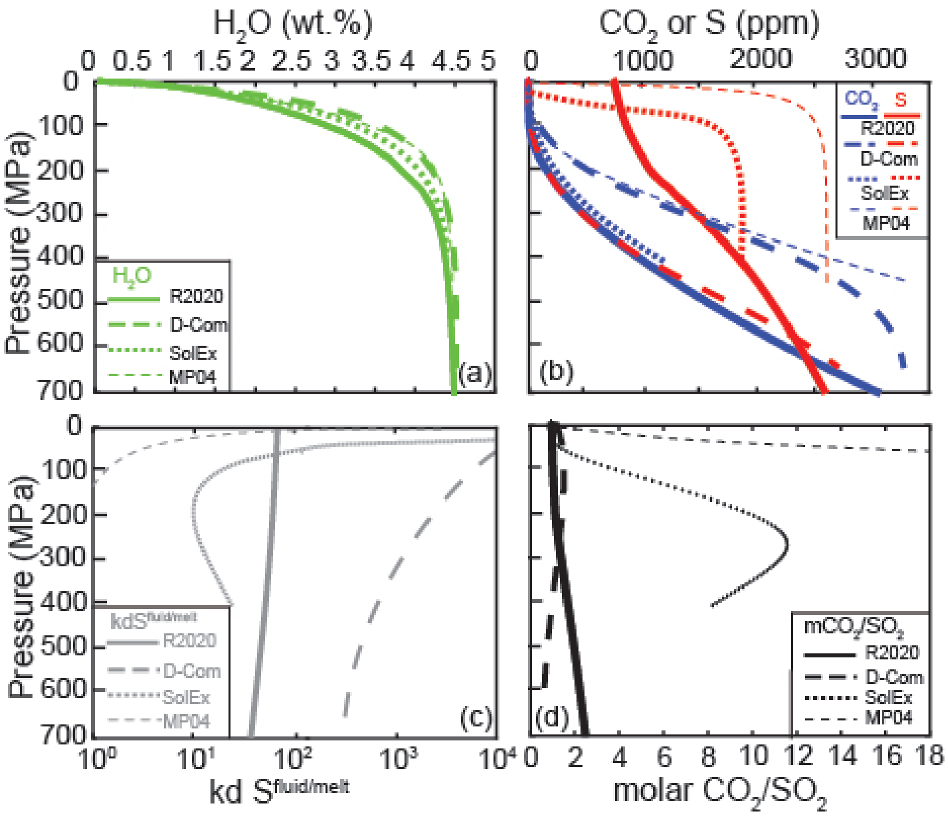

Figure 3. (a) H_2O (green), (b) CO_2 (blue) and S (red) evolution in the melt during decompression degassing using D-Compress (Burgisser et al., 2015), SolEx (Witham et al., 2012), MP04 (Moretti and Papale, 2004) and an empirical model that fits Fuego, R2020 (Rasmussen et al., 2020). (c) Calculated partition coefficients of S between fluid and basaltic melt from four models. (d) Molar CO_2/SO_2 ratios in the coexisting vapor for the same three models in (a) and (b). R2020, D-Compress and MP04 start with 4.5 wt.% H_2O, 3300 ppm CO_2, and ~2600 ppm S. SolEx is forced to start at 400 MPa, the highest pressure that can be applied in the model, with 4.3 wt.% H2O, ~1100 ppm CO_2 and 2100 ppm S.

Because silicate melts are never saturated in a pure sulfur vapor or fluid phase (a solid or immiscible melt phase saturates before this state can occur), the sulfur distribution between the fluid and melt can also be described by a partition coefficient ($k_d(S)^{v/m}$). Therefore, a common method of modeling COHS degassing is to couple an existing COH degassing model (e.g., VolatileCalc) with a sulfur partitioning model (Sisson and Layne, 1993; Burton et al., 2007;

Johnson et al., 2010; Witham et al., 2012; Gennaro et al., 2020; Rasmussen et al., 2020). The employed $k_d(S)^{v/m}$ are usually based on experimental studies (Burton et al., 2007; Witham et al., 2012; Gennaro et al., 2020) or empirically determined from melt inclusion data (Sisson and Layne, 1993; Johnson et al., 2010; Rasmussen et al., 2020). For example, the solid curves in Figure 1 and Figure 3 are results of an empirical fit of the rehomogenized melt inclusions by Rasmussen et al. (2020) that combines the COH degassing results from VolatileCalc and a fixed bulk partition coefficient for sulfur ($D_S^{non-melt/melt} = kd_S^{v/m} \times \frac{X_v}{X_v+X_{min}} + kd_S^{min/m} \times \frac{X_{min}}{X_v+X_{min}} = 4$) between non-melt phases (vapor + minerals) and silicate melt. Unlike most of the degassing models of this kind and other forward thermodynamic models that only consider melt and vapor in the system, Rasmussen et al. (2020) includes crystallization and predicts that $k_d(S)^{v/m}$ increases from 20 to 60 as melt fraction decreases from 100% to 40% along the coupled decompression, degassing, and differentiation path. Existing experiments show that $k_d(S)^{v/m}$ is a function of temperature, pressure, melt composition, and oxygen fugacity (Webster and Botcharnikov, 2011). Except for SolEx, $k_d(S)^{v/m}$ in empirical models is tailored to fit the melt inclusion data from a specific volcano, meaning it cannot easily be applied to other systems. However, the forward model SolEx (Witham et al., 2012) fails to produce the CO_2-S degassing trend in Figure 1, which is likely due to several issues with the experiments used to parameterize the model's sulfur partition coefficients (Lesne et al., 2011) that are discussed below.

Table 1 Previous Degassing mode

Model	S behavior	fO_2	*P (MPa)*	References
D_Compress	$w_{S^{2-}} = a_{H_2S} \times {f_{H_2S}}^{b_{H_2S}}$ $w_{S^{6+}} = a_{SO_2} \times {f_{SO_2}}^{b_{SO_2}}$	change	25-200	Burgisser et al. (2015)
M&P	$C_{S^{2-}} = w_{S^{2-}} \times ({}^{fO_2}/_{fS_2})^{1/2}$ $C_{SO_4^{2-}} = w_{S^{6+}} \times fO_2^{-3/2} \times fS_2^{-1/2}$	fixed	0.0001	Moretti and Papale (2004)
SolEx	$kd_S^{fl/melt} = w_S^{fluid} / w_S^{melt}$	Oxidized only	25-400	Witham et al. (2012)
Emprical models	$kd_S^{fl/melt} = w_S^{fluid} / w_S^{melt}$	Tailored for one volcano	-	

The evolution of *fO₂* during magma degassing also represents a challenge to most existing models. Empirical models employ bulk sulfur partition coefficients and do not consider sulfur speciation or redox change, meaning they can only be applied to systems with similar fO_2. For example, sulfur partition coefficients implemented in SolEx were empirically parameterized from experiments with fO_2 between NNO+1.6 and NNO+2.1 (Witham et al., 2012). The Moretti and Papale (2004) model considers both SO_2 and H_2S in the gas at a given fO_2 using the gas equilibrium reaction described in equation 2 and then uses the calculated fSO_2 and fH_2S and sulfate and sulfide capacity to calculate the quantity of S^{6+} and S^{2-} in the melt. However, the lack of experiments constraining the sulfate and sulfide capacity at pressures higher than 1 atm can compromise the S^{6+} and S^{2-} calculation. Also, the model can only be run at a fixed fO_2 along the degassing path. D-Compress considers the evolution of redox states of the system based on multiple equilibria involving C, O, H, and S-bearing species in the vapor and the ferrous and ferric iron in the magma (Burgisser et al., 2015). This model has been used to describe redox evolution in different magmatic systems (Burgisser and Scaillet, 2007; Moussallam et al., 2016; Longpré et al., 2017) and atmosphere evolution at planetary surfaces (Gaillard et al., 2011; Gaillard and Scaillet, 2014; Liggins et al., 2020). However, because it does not consider S-Fe redox equilibrium in the silicate melt, D-Compress may not accurately predict fO_2 evolution. A recent degassing model from Hughes et al (in review) tracks the fO_2 evolution during degassing with a similar strategy as D-Compress and calculates S^{6+} and S^{2-} in the melt using fSO_2 and fH_2S, and sulfate and sulfide capacities. However, it is also limited by a lack of experimental constraints on sulfate and sulfide capacities at pressures higher than 1 atm. None of the models above directly consider the S-Fe redox equilibrium in the melt, or S redox equilibrium between melt and vapor. Instead, the fO_2 evolution in the system is entirely controlled by the equilibrium reactions among multiple gas species. $Fe^{3+}/\Sigma Fe$ in the melt only responds to the calculated fO_2, and $S^{6+}/\Sigma S$ in the melt is determined by fSO_2 and fH_2S, either through solubility laws that are a function of the corresponding species fugacities (Burgisser et al., 2015) or sulfate and sulfide capacities (Hughes et al., in review).

2.3 Previous S partitioning experiments

$k_d(S)^{v/m}$ has been investigated in previous experimental studies of basaltic-andesitic systems under controlled fO_2 from FMQ-1 to FMQ+4, T of 900-1400 °C, and P of 0.1-500 MPa (O'Neill and Mavrogenes, 2002; Moune et al., 2008; Lesne et al., 2011; Zajacz et al., 2012; Zajacz et al., 2013; Fiege et al., 2014a; Zajacz, 2014; Fiege et al., 2015; Masotta et al., 2016; Nash et al., 2019; Gennaro et al., 2020). However, due to the multiple redox states of sulfur in the melt and vapor, the paucity of experiments at pressures higher than 300 MPa, and the technical difficulties in conducting S-bearing hydrothermal experiments (Webster and Botcharnikov, 2011), there is no existing thermodynamic or empirical model to predict $k_d(S)^{v/m}$ in the basaltic-andesitic system across reduced and oxidized condition. This is the goal of this paper.

Existing experiments conducted at pressures >1 atm show complex variations in $k_d(S)^{v/m}$ with increasing fO_2 (Fig. 2b). In experiments with S^{2-} only in the melt, $k_d(S)^{v/m}$ increases with increasing fO_2 from FMQ to FMQ +1, while in experiments with S^{6+} only, $k_d(S)^{v/m}$ decreases with increasing fO_2 from FMQ+1.5 to FMQ+4. Previous experiments have shown that S bonds with different cations in the silicate melt depending on its speciation (S^{2-} or S^{6+});$^-$), hence, $k_d(S)^{v/m}$ is affected by various compositional factors at different fO_2 (Zajacz, 2014; Fiege et al., 2015; Masotta et al., 2016). Under oxidized conditions, where S exists only as SO_4^{2-} and bonds with Ca^{2+}, K^+, and Na^+, $k_d(S)^{v/m}$ is affected by NBO/T (non-bridging oxygen) and the abundance of cations (Ca^{2+}, K^+, and Na^+) over what is required to charge balance Al–Si complexes in the silicate melt structure (Zajacz, 2014; Masotta et al., 2016). At reduced conditions, when S^{2-} is dominant in the melt and bonds with Fe^{2+}, $k_d(S)^{v/m}$ decreases as $Fe^{2+}O$ increases (Fiege et al., 2015). Thus, there is no universal model for $k_d(S)^{v/m}$ that can capture the behavior of the different melt and vapor species of S in all the experiments across the range of fO_2 and melt compositions.

Pressure is another important factor. Recent studies have used multiple approach to reconstruct the CO_2 concentration in melt inclusions that have lost CO_2 to shrinkage bubbles (Steele-Macinnis et al., 2011; Esposito et al., 2012; Hartley et al., 2014; Mironov et al., 2015; Moore et al., 2015; Wallace et al., 2015; Aster et al., 2016; Rasmussen et al., 2017; Steele-MacInnis et al., 2017; Moore et al., 2018; Rasmussen et al., 2020). The reconstructions not only dramatically increase estimates for the CO_2 concentration in the melt inclusions, but also enhance the estimates of the depths where arc magma likely starts degassing due to the higher pressures required for higher CO_2 melt concentrations. In particular, the co-variation of S and CO_2 in rehomogenized melt inclusion records from the Fuego 1974 eruption shows that S likely degassed together with CO_2 at high pressure in the magma that fed this eruption. The empirical fit of the Fuego rehomogenized melt inclusions from Rasmussen et al. (2020) shows that almost half of the sulfur could have already degassed at pressures > 300 MPa. Most experiments constraining $k_d(S)^{v/m}$, however, have been conducted at pressure of 200 MPa or lower (O'Neill and Eggins, 2002; Moune et al., 2008; Zajacz et al., 2012; Fiege et al., 2014a; Masotta et al., 2016; Nash et al., 2019). Zajacz (2014) conducted experiments at 500 MPa to constrain the effect of melt composition on $k_d(S)^{v/m}$. However, the experiments were performed using synthetic melt compositions with extremely high Na_2O (> 10 wt.%), CaO (>20 wt.%), or K_2O (> 5wt.%), which makes them inappropriate to directly apply to terrestrial basaltic melts. Lesne et al. (2011) conducted a series of extremely challenging partitioning experiments involving melt and COHS vapor from 50 to 400 MPa. However, large uncertainties in mass balance calculations caused by minimal S loss to the fluid in some experiments, significant S loss to the AuPd capsules in others, as well as underestimates of fO_2, and hydrogen loss through the capsule wall could have compromised the derived $k_d(S)^{v/m}$. Experiments on Stromboli compositions at pressures higher than 150 MPa from Lesne et al. (2011) showed almost no sulfur loss to the vapor phase within the S analytical errors of EPMA. On the contrary, experiments on a Masaya volcano melt composition displayed a S increase as pressure decreased from 400 MPa to 150 MPa (Figure 3d in Lesne et al., 2011), then a decrease as pressure continues decreasing. However, the increase in the S concentration of the melt from 400MPa to 150 MPa is accompanied by a decrease in run duration, which is consistent with increasing sulfur loss to the AuPd as run duration increases. Last but not least, as pointed out by Burgisser et al. (2015), the fO_2 in the experiments from Lesne et al. (2011) might be much lower than what was reported due to Fe reduction induced by hydrogen loss through the capsule wall. The more reduced system could also have been responsible for S loss to the AuPd capsule as S^{2-}. All three scenarios hinder the mass balance calculations of sulfur contents in the vapor. As a result, $k_d(S)^{v/m}$ derived from mass balance calculation by Lesne et al (2011) have considerable uncertainty, mainly for experiments at pressures higher than 150 MPa. Since the sulfur degassing model in SolEx is exclusively derived from experiments from Lesne et al (2011), it is not surprising that SolEx does not reproduce the CO_2-S degassing trend demonstrated by rehomogenized melt inclusions.

Formation of sulfide or sulfate minerals can also reduce the experimentally constrained $k_d(S)^{v/m}$. Even trace amounts of sulfide or sulfate precipitation could account for a non-negligible amount of sulfur. Such sulfur loss is difficult to quantify and in mass balance calculations gives the appearance that there is more S lost to vapor than actually occurred. In this case, the derived $k_d(S)^{v/m}$ can only be considered a maximum value (Gennaro et al., 2020) and therefore is not ideal to use for model calibration.

3. A NEW DEGASSING MODEL: Sulfur_X

The approach adopted in this study combines existing COH degassing models (Newman and Lowenstern, 2002; Iacono-Marziano et al., 2012) with sulfur partition coefficients to predict the evolution of S, CO_2, and H_2O in basaltic melt and co-existing vapor. To tackle the challenges of different sulfur species, we consider three sulfur degassing reactions and develop predictive models of $k_d(S)^{v/m}$ for each reaction guided by relevant published experimental data. The consideration of $k_d(S)^{v/m}$ for each reaction also allows us to estimate thermodynamic properties of components in the reactions using solid analogs, both as a guide to empirical fitting of the experimental data and to interpolate and extrapolate the pressure and temperature effects beyond the *P-T* range of existing experiments.

3.1 Three $k_d(S)^{v/m}$

Sulfur can exist in the melt as $S^{2-}$and S^{6+} (Jugo et al., 2010), and as SO_2 and H_2S in the co-existing vapor. Figure 2a shows S speciation in the melt and in the vapor as a function of fO_2

with temperature between 1050°C and 1300°C (Nash et al., 2019; Muth and Wallace, 2021). When the magma is reduced (< FMQ), S^{2-} is the dominant melt species and H_2S is the dominant vapor species. In this case, the sulfur degassing reaction can be described as:

$$FeS_{melt} + H_2O_{vapor} = H_2S_{vapor} + FeO_{melt} \qquad \text{(RxnI, 4)}$$

Fe^{2+} is included in this reaction because previous studies have demonstrated that S^{2-} preferably bonds with Fe^{2+} in the silicate melt (Haughton et al., 1974; Righter et al., 2009; Ding et al., 2014). When the magma is very oxidized (> FMQ+2.5), S^{6+} and SO_2 are the dominant sulfur species in the melt and vapor, respectively. In this case, the sulfur degassing reaction can be written as:

$$CaSO_{4,\ melt} = SO_{2,vapor} + CaO_{melt} + 0.5O_{2,\ vapor} \qquad \text{(RxnII, 5)}$$

Ca^{2+} is representative of one of the important cations bonding with SO_4^{2-} in the silicate melt (Zajacz, 2014), and we note that similar expressions could be written involving other important cations such as K^+ and Na^+.

However, within the range of *fO₂* relevant to arc magmas, between FMQ and FMQ+2 (Figure 3a), both S^{2-} and S^{6+} exist in the melt and both SO_2 and H_2S in the vapor, and the transitions from S^{2-} to S^{6+} in the melt and from H_2S to SO_2 in the vapor may not be synchronized at the same fO_2 (Fig. 2). In this case, two S species are present in the melt and two S components are present in the vapor, and therefore S degassing involves four relevant equilibria. In addition to RxnI and RxnII above, S^{2-} may also degas to SO_2 (RxnIa) and S^{6+} may degas to H_2S (RxnIIa):

$$FeS_{melt} + 1.5O_{2,\ vapor} = SO_{2,vapor} + FeO_{melt} \qquad \text{(RxnIa, 6)}$$

$$CaSO_{4,melt} + H_2O_{melt} = 2O_{2,\ vapor} + H_2S_{vapor} + CaO_{melt} \qquad \text{(RxnIIa, 7)}$$

Therefore, we tackle this complexity by considering $k_d(S)^{v/m}$ for each reaction individually, and calibrate using subsets of experimental data for conditions where one of the melt species and one of the vapor species dominate. We then combine all partition coefficients into a single, effective bulk $k_d(S)^{v/m}$ value weighted by the speciation of sulfur in the melt and the vapor. We show that this empirical method successfully reproduces melt inclusion CO_2-S variations.

As shown in the following discussion, no existing experiments involve the combination of S species in RxnIIa (supplementary Table 1), and thus, it might not be as important as the other three reactions within the fO_2-T-fH_2O range of interest. The lack of experiments would also make it difficult to calibrate $kdS_{RxnIIa}^{fl/m}$. Therefore, in our degassing model we only consider RxnI, RxnIa, and RxnII. To explore the factors that affect each reaction, we first write the equilibrium constants for each reaction.

$$K_{RxnI}(P,T) = \frac{f_{H_2S}\, a_{FeO}}{a_{FeS} f_{H_2O}} = K_{RxnI}^{0} \exp\left(\frac{-\Delta V_{P_0,T_0}(P-P_0)}{RT} + \frac{-\Delta H_{P_0,T_0}}{R}\left(\frac{1}{T}-\frac{1}{T_0}\right)\right) \tag{8}$$

$$K_{RxnIa}(P,T) = \frac{f_{SO_2}\, a_{FeO}}{a_{FeS} f_{O_2}^{3/2}} = K_{RxnIa}^{0} \exp\left(\frac{-\Delta V_{P_0,T_0}(P-P_0)}{RT} + \frac{-\Delta H_{P_0,T_0}}{R}\left(\frac{1}{T}-\frac{1}{T_0}\right)\right) \tag{9}$$

$$K_{RxnII}(P,T) = \frac{f_{SO_2}\, a_{CaO}\, f_{O_2}^{1/2}}{a_{CaSO_4}} = K_{RxnII}^{0} \exp\left(\frac{-\Delta V_{P_0,T_0}(P-P_0)}{RT} + \frac{-\Delta H_{P_0,T_0}}{R}\left(\frac{1}{T}-\frac{1}{T_0}\right)\right) \tag{10}$$

where f represents fugacity and can be expressed as the product of pressure, fugacity coefficient, and the mole fraction (e.g., $f_{SO_2} = P\ \varphi_{SO_{2,v}}\ X_{SO_{2,v}}$); a is the activity of the components in the silicate melt and can be expressed as the product of the activity coefficient and the mole fraction (e.g., $a_{FeO} = \gamma_{FeO_{melt}}\ X_{FeO_{melt}}$); and K^0, $\Delta V_{P_0,T_0}$, and $\Delta H_{P_0,T_0}$ are the equilibrium constant, molar volume change of the incompressible components in the reaction and enthalpy change of the reaction at reference pressure (P_0) and temperature (T_0)(e.g., see Stolper and Holloway, 1988)). The values for $kdS_{RxnI}^{v/m}$, $kdS_{RxnII}^{v/m}$, and $kdS_{RxnIa}^{v/m}$ as molar ratios can be expressed (e.g.,

$kdS^{v/m}_{RxnI} = {X_{H_2S_v}}/{X_{S^{2-}_{melt}}}$) by rearranging the equilibrium constant expressions above and assuming that $X_{FeS_{melt}} = X_{S^{2-}_{melt}}$ in RxnI and Ia, and $X_{CaSO_{4,melt}} = X_{S^{6+}_{melt}}$ in RxnII.

$$ln\left(kdS^{\frac{vapor}{melt}}_{RxnI}\right) = \ln\left(\frac{X_{H_2S vapor}}{X_{S^{2-}_{melt}}}\right) = \ln K^0_{RxnI} + \frac{-\Delta V\ (P - P_0)}{RT} + \frac{-\Delta H_{T_0}}{R}\left(\frac{1}{T} - \frac{1}{T_0}\right) + lnf_{H_2O} - \ln X_{\mathrm{FeO}} - \ln\gamma FeO - \ln \mathrm{P} - \ln\varphi H2S + ln\gamma_{FeS} \qquad (11)$$

$$\ln\ (kdS^{\frac{vapor}{melt}}_{RxnIa}) = \ln\left(\frac{X_{SO_{2,vapor}}}{X_{S^{2-}_{melt}}}\right) = \ln K^0_{RxnIa} + \frac{-\Delta V\ (P - P_0)}{RT} + \frac{-\Delta H_{T_0}}{R}\left(\frac{1}{T} - \frac{1}{T_0}\right) + \frac{3}{2} lnf_{O_2} - \ln X_{\mathrm{FeO}} - \ln\gamma_{FeO} - \ln \mathrm{P} - \ln\varphi_{SO_2} + ln\gamma_{FeS} \qquad (12)$$

$$\ln\ (kdS^{\frac{vapor}{melt}}_{RxnII}) = \ln\left(\frac{X_{SO_{2,vapor}}}{X_{S^{6+}_{melt}}}\right) = \ln K^0_{RxnII} + \frac{-\Delta V\ (P - P_0)}{RT} + \frac{-\Delta H_{T_0}}{R}\left(\frac{1}{T} - \frac{1}{T_0}\right) - 0.5 lnfO_2 - \ln \mathrm{P} - \ln\varphi_{SO_2} + \ln a_{CaO} + ln\gamma_{CaSO_4} \qquad (13)$$

In equations (11-13), f_{H_2O}, f_{O_2} and X_{FeO} are known from the experiments, φ_{H_2S} and φ_{SO_2} are calculated from the equation of states (Shi and Saxena, 1992), and γ_{FeO} is calculated by the empirical model of O'Neill and Eggins (2002). ΔV and ΔH_{T_0} for each reaction can either be regressed from the experiments accordingly (e.g., Stolper and Holloway, 1988) or estimated using the thermodynamic properties of their solid analogs (JANAF), although we note that O'Neill (2021) cautioned against the latter approach. There are no previous constraints on the activity coefficients, γ_{FeS}, γ_{CaSO_4}, and γ_{CaO} in relevant melts. We derive empirical expressions for these three terms using the experimental data available for each reaction. Such empirical expressions include several compositional terms that also include the effects of other melt species that potentially could bind with S^{2-} and S^{6+}. The separation of sulfur degassing into these three reactions clearly shows that fO_2 does not have a monotonic effect on $k_d(S)^{v/m}$, and it confirms the experimental observation that different compositional factors on $k_d(S)^{v/m}$ are important depending on the degassing reaction that is dominant. We note that although we have chosen to empirically calibrate the three $k_d(S)^{v/m}$ values separately, the final implementation in Sulfur_X uses a single, effective bulk $k_d(S)^{v/m}$ value weighted by the speciation of sulfur in the melt and vapor, and the final model achieves equilibrium in melt and vapor by coupling of melt Fe-S redox equilibrium and vapor SO_2-H_2S equilibrium.

To derive $k_d(S)^{v/m}$ for each reaction, we examine existing $k_d(S)^{v/m}$ experiments on basalts and basaltic andesites and ascribe them as relevant to RxnI, RxnIa, or RxnII, depending on the sulfur speciation in the melt and the vapor (Table 2). Experiments reported as sulfide or sulfate saturated (O'Neill and Mavrogenes, 2002; Beermann et al., 2011; Botcharnikov et al., 2011a; Gennaro et al., 2020) are not considered so as to minimize the errors involved in the reported $k_d(S)^{v/m}$. This is a limitation of our degassing model, and future work will include a solid or immiscible sulfide or sulfate phase. Experiments without reliable determination of fO_2 or sulfur speciation (Lesne et al., 2011) are not considered because they cannot be used to constrain the effect of fO_2 on individual $k_d(S)^{v/m}$. Applying the two criteria above, we use the experiments from Fiege et al., (2015), Moune et al. (2008), Nash et al. (2019), O'Neill and Mavrogenes (2002), Zajacz (2014), and Zajacz et al. (2013, 2012) to constrain the $k_d(S)^{v/m}$ for each reaction. Some experimental studies report S speciation in the melt as determined by XANES (Fiege et al., 2014c; Nash et al., 2019), EPMA using the SK_α peak shift method, or Raman spectroscopy (Zajacz, 2014) whereas other experimental studies report only experimental fO_2. Therefore, S speciation in each experiment is either taken from the direct $S^{6+}/\Sigma S$ measurements or calculated by Nash et al. (2019) when no $S^{6+}/\Sigma S$ measurements are available. The SO_2/H_2S ratio in the vapor for each experiment is calculated from the gas equilibrium equation (3).

Table 2 Experiments for $k_d(S)^{fl/m}$ calibration

$kdS^{v/m}_{RxnI}$ ($FeS_{melt} - H_2S_{vapor}$)								
References	N[a]	*P (MPa)*	*T °C*	fO_2[b]	Composition	SO_2/S_T in the vapor[c]	S^{6+}/S_T in the melt[d]	Experiment methods
Fiege et al. (2015)	2	70	1050	-0.07 -0.03	basalt	H_2S (+H_2O)	0,0.11	IHPV, controlled fO_2
Moune et al. (2008)	8	200, 300	1050	(-0.1) ~0.3	basalt	H_2S (+H_2O)	0	IHPV, controlled fO_2
Zajac et al. (2012, 2013)	12	185, 200	1000, 1030	0, 0.2	Andesite	H_2S (+H_2O)	0	IHPV, controlled fO_2
$kdS^{v/m}_{RxnII}$ ($CaSO_{4,melt} - SO_{2,vapor}$)								
Fiege et al 2015	11	70	1150, 1200	4.1	basalt	SO_2(+H_2O)	1	IHPV, fO_2 controlled
Zajac (2014)	23	500	1240	2.1	sythesized composition with abnormal $Na_2O/CaO/MgO$	>0.98 SO_2 (H_2S+H_2O)	0.98-1	IHPV, fO_2 controlled
Zajac et al. (2012)	2	200	1000	2.54	andesite	SO2>96%	1	IHPV, fO_2 controlled
Nash et al. (2019)	7	0.1	1300	1.08-1.5	basalt-dacite	SO_2 (CO, CO_2, S_2, COS)	0.95-1	CO_CO_2_SO_2 gas mixing
$kdS^{v/m}_{RxnIa}$ ($FeS_{melt} - SO_{2,vapor}$)								
Fiege et al. (2015)	8	70	1050, 1200	0.08 ~1.17	basalt	0.12-0.86 SO_2 (+H_2O)	0-0.11	IHPV, fO_2 controlled
O'Neill and Mavrogenes (2002)	9	0.1	1400	(-4)~-1	basalt-dacite	0.94 SO_2(CO, CO2, COS, S_2)	0	CO_CO_2_SO_2 gas mixing
Nash et al. (2019)	16	0.1	1300	(-1.76)-0	basalt-dacite	SO_2 (CO, CO_2, COS, S_2)	0	CO_CO_2_SO_2 gas mixing

[a] N is the number of experiments used for regression.

[b] fO_2 is reported by each experimental study and all are recalculated to be relative to FMQ buffer here.

[c] SO_2/S_T in the vapor is calculated by equation (3) in the main text using the experimental temperature, pressure and fO_2

[d] S^{6+}/S_T in the melt is reported in Fiege et al. (2015) and Nash et al. (2019). The rest is calculated using Nash et al. (2019) and experimental temperature.

With the calculated or measured S speciation in the melt and the calculated sulfur speciation in the vapor, we were able to categorize experiments as relevant to RxnI, RxnIa, and RxnII. For RxnI and RxnII, experiments with only S^{2-} or S^{6+} in the melt, and with only H_2S or dominantly SO_2 (>90%) in the vapor are used, respectively. For RxnIa, ideally, experiments would be reported with S^{2-} only in the melt and SO_2 only in the vapor. However, few experiments meet such criteria (O'Neill and Mavrogenes, 2002; Nash et al., 2019), particularly at pressures higher than 1 atm. Therefore, we also included experiments with less than 10% S^{6+} in the melt and less than 40% H_2S in the vapor into the RxnIa category. Given the errors that might have been introduced in recalculating the $kdS^{v/m}_{RxnIa}$ by using the calculated $S^{6+}/\Sigma S$ in the melt and SO_2/H_2S in the vapor, we used the $k_d(S)^{v/m}$ reported in those experiment as the $kdS^{v/m}_{RxnIa}$. Given that non-negligible H_2S is included in some of these experiments, the $kdS^{v/m}_{RxnIa}$ can be considered as a maximum and naturally, larger errors are involved in this set of experiments. Reference temperature and pressure of each reaction were chosen to be the *P-T* conditions at which most of the relevant experiments were done, for simplicity. The *P-T-*fO_2 conditions of experimental studies used to calibrate the $kdS^{v/m}_{RxnI}$, $kdS^{fl/m}_{RxnII}$, and $kdS^{v/m}_{RxnIa}$ are listed in Table 2. Details of each experiment from these studies are given in supplementary Table 1.

Experiments within each reaction group span pressure and temperature ranges too small to determine statistically meaningful volume (ΔV) and enthalpy (ΔH_{T_0}) changes by regression. Therefore, we used thermodynamic properties of each component or their solid analogs for estimating the enthalpy changes. ΔH_{T_0} for RxnI and RxnIa are calculated at the relevant value of T_0 using the enthalpies of their solid analogues and the vapor components from JANAF (supplementary Fig. 1a). Fiege et al. (2015) constrained the temperature dependence of $k_d(S)^{v/m}$ at oxidized condition (FMQ+4) with three sets of basaltic compositions from 1150 to 1250 °C.

Therefore, for RxnII, we adopted a value for ΔH_{T_0} regressed from these T-series experiments (supplementary Figure 1b), and the result is of the same order of magnitude as the value calculated using the thermodynamic properties of the solid analogues and vapor components from JANAF (44828 KJ vs. 32379 KJ).

In equations 11 and 12, $\Delta V_{RxnI\ and\ RxnIa} = V_{mole}^{FeO,\,melt} - V_{mole}^{FeS,\ \ sulfide\,melt}$(Kress and Carmichael, 1991; Kress et al., 2008). We assume that the value for ΔV is independent of *T* and *P*. The molar volume change of RxnII, $\Delta V_{RxnII} = V_{mole}^{SO_4^{2-},\,melt} - V_{mole}^{O^{2-},\,melt}$, is more difficult to assess. We made an estimate based on a comparison with dissolution of CO_2 as CO_3^{2-} in basaltic melts. Stolper and Holloway (1988) described CO_2 solubility using the following reaction:

$$CO_{2,vapor} + O_{melt}^{2-} = CO_{3,melt}^{2-}$$

Using regression of experimental solubility data, they found $\Delta V_r^{0,melt} = \left(V_{CO_3^{2-}}^{0,melt}\right) - \left(V_{O^{2-}}^{0,melt}\right) = 33.0 \pm 0.5\ \text{cm}^3/\text{mole}$, where $V_{O^{2-}}^{0,melt}\ and\ V_{CO_3^{2-}}^{0,melt}$are the partial molar volumes of these species in the melt. We assume that the pressure dependence for RxnII can be approximated using an alternate form of RxnII:

$$SO_{4,melt}^{2-} = SO_{2,vapor} + O_{melt}^{2-} + 0.5O_{2,vapor}$$

for which $\Delta V_r^{0,melt} = \left(V_{O^{2-}}^{0,melt}\right) - \left(V_{SO_4^{2-}}^{0,melt}\right)$. If the volume change for the carbonate dissolution reaction results mainly from the difference of $2O^{2-}$, then we can estimate the volume change for RxnII, which has a $3O^{2-}$ difference, as ΔV_{RxnII} = 1.5 * 33 = 49.5 cm^3/mole. Reference temperature and pressure, and all the thermodynamic properties at the reference *P*-*T* used for each reaction are listed in Table 3.

The last terms to be determined are the equilibrium constants for each reaction and the activity coefficients of FeS, $CaSO_4$, and CaO in the melt. Since S^{2-} bonds with Fe^{2+}, and potentially with H^+ to form HS^-, we considered X_{FeO} and ${X^2}_{H_2O}$ as two compositional terms affecting γ_{FeS}, where X is the mole fraction calculated on a single cation base. RxnI experiments with 3-6 wt.% water and 5-14 wt.% FeO in the melt were used to regress for $\ln K^0_{RxnI}$ and for coefficients making γ_{FeS} a function of X_{FeO} and ${X^2}_{H_2O}$ after moving all the other terms to the left side of equation (4). The regression is done by the Inverse Iterative Least Squares Method (details in the supplementary materials). Since both RxnI and RxnIa share γ_{FeS}, we applied the γ_{FeS} derived from RxnI experiments to RxnIa. $\ln K^0_{RxnIa}$ is averaged from the residues of 30 RxnIa experiments after moving all the known parameters to the left side of the equation (5).

Zajacz (2014) investigated different compositional terms that can affect the partition coefficient of sulfur under oxidized conditions relevant for RxnII. Among the terms, excess Ca$(2X_{Ca} - X_{Al})$, excess Na$(X_{Na} - X_{Al})$, and the non-bridging oxygen (NBO/T) show good correlations with the $kdS^{v/m}_{RxnII}$ for experiments in the RxnII group after accounting for the effects of fO_2, pressure and temperature. Therefore, 2Ca-Al, Na-Al, and NBO/T were used to represent the combined compositional effects on γ_{CaSO_4} and γ_{CaO}, and the coefficients of each compositional term were regressed using the 45 experiments in RxnII group by the Inverse Iterative Least Squares Method (Supplementary Material). The final equations for $kdS^{v/m}_{RxnI}$, $kdS^{v/m}_{RxnIa}$ and $kdS^{v/m}_{RxnII}$, the parameters and regressed coefficients for each of the compositional terms, and the equilibrium constants are all listed in Table 3. The individual effects of pressure, temperature, oxygen fugacity, and different compositional components on $kdS^{fl/m}_{RxnI}$ and $kdS^{fl/m}_{RxnIa}$ are plotted in supplementary Figure 2; on $kdS^{fl/m}_{RxnII}$ in supplementary Figure 3.

Table 3 $k_d(S)^{v/m}$ from this study

<table>
<tr><td colspan="8">RxnI: $\ln\left(\frac{XH_2S_{vapor}}{XS_{melt}}\right) = \ln K^0_{RxnI} + \frac{-\Delta V\,(P-P_0)}{R\times T} + \frac{-\Delta H_{T_0}}{R}\left(\frac{1}{T}-\frac{1}{T_0}\right) + lnfH_2O - \ln XFeO - \ln\gamma FeO - \ln P - \ln\varphi H2S + AXFeO + B(X2O)^2$</td></tr>
<tr><td>$P_0\ (MPa)$</td><td>T_0 (°C)</td><td>$\Delta V\ (cm^3/mol)$</td><td>ΔH_{T_0}</td><td>$\ln K^0_{RxnI}$</td><td>A</td><td>B</td><td></td></tr>
<tr><td>100</td><td>1100</td><td>-9.42</td><td>44827.65</td><td>0.616843
(0.492902)</td><td>-8.715144
(4.250800)</td><td>20.844254
(4.395644)</td><td></td></tr>
<tr><td colspan="8">RxnIa: $\ln\left(\frac{XSO_{2,vapor}}{XS_{melt}}\right) = \ln K^0_{RxnIa} + \frac{-\Delta V\,(P-P_0)}{R\times T} + \frac{-\Delta H_{T_0}}{R}\left(\frac{1}{T}-\frac{1}{T_0}\right) + \frac{3}{2}\times lnfO_2 - \ln XFeO - \ln\gamma FeO - \ln P - \ln\varphi SO_2 + AXFeO + B(X2O)^2$</td></tr>
<tr><td>$P_0\ (MPa)$</td><td>T_0 (°C)</td><td>$\Delta V\ (cm^3/mol)$</td><td>ΔH_{T_0}</td><td>$\ln K^0_{RxnIa}$</td><td>A</td><td>B</td><td></td></tr>
<tr><td>100</td><td>1400</td><td>-9.42</td><td>-476704</td><td>29.79217
(0.703081)</td><td>-8.715144
(4.250800)</td><td>20.844254
(4.395644)</td><td></td></tr>
<tr><td colspan="8">RxnII: $\ln\left(\frac{XSO_{2,vapor}}{XS_{melt}}\right) = \ln K^0_{RxnII} + \frac{-\Delta V\,(P-P_0)}{R\times T} + \frac{-\Delta H_{T_0}}{R}\left(\frac{1}{T}-\frac{1}{T_0}\right) - 0.5\times lnfO_2 - \ln P - \ln\varphi SO_2 + A(2Ca - Al) + B\frac{NBO}{T} + C(Na - Al)$</td></tr>
<tr><td>$P_0\ (MPa)$</td><td>T_0 (°C)</td><td>$\Delta V\ (cm^3/mol)$</td><td>ΔH_{T_0}</td><td>$\ln K^0_{RxnII}$</td><td>A</td><td>B</td><td>C</td></tr>
<tr><td>200</td><td>1000</td><td>49.5</td><td>32379</td><td>-0.255609
(0.092976)</td><td>-9.888169
(0.477521)</td><td>-0.970780
(0.175012)</td><td>-24.763957
(0.658748)</td></tr>
</table>

Figure 4 shows the comparisons between the predicted and the measured partition coefficients for RxnI (Fig. 4a), RxnIa (Fig.4b, 4c), and RxnII (Fig. 4d, 4e). Most experiments in RxnI and RxnII can be reproduced by the $kdS^{v/m}_{RxnI}$ and $kdS^{v/m}_{RxnII}$ models within 20%, while greater discrepancies are displayed in $kdS^{v/m}_{RxnIa}$, likely because of the more significant uncertainties in the experimental determination of $kdS^{v/m}_{RxnIa}$ as discussed above. In addition, $kdS^{v/m}_{RxnIa}$ and $kdS^{v/m}_{RxnII}$ that are determined from the experiments in Fiege et al. (2015) are systematically over- and under-estimated, respectively, by our expressions. This could be explained by a slight overestimate of *fO_2* of these experiments. For example, the predicted $kdS^{v/m}_{RxnIa}$ are within 30% of the observed $kdS^{v/m}_{RxnIa}$ if *fO_2* is 0.25 log unit lower (Fig. 4c). This slight shift of *fO_2* is within the error (± 0.5 log unit) reported in Feige et al. (2015). $kdS^{v/m}_{RxnIa}$ has the same calibration error derived from regression with $kdS^{v/m}_{RxnI}$ because they share the same compositional factors (X_{FeO} and $X^2{}_{H_2O}$) used to calculate γ_{FeS}. The calculated errors for ln $(kdS^{\frac{v}{m}}_{RxnI})$ and ln $(kdS^{\frac{v}{m}}_{RxnIa})$regressions are estimated to be ±0.444004, and ln$(kdS^{v/m}_{RxnII})$ to be ±0.293387, which translate to 40% uncertainties of predicted $kdS^{fl/m}_{RxnI}$ and $kdS^{v/m}_{RxnIa}$, and 22% of predicted $kdS^{fl/m}_{RxnII}$, respectively. More details on the error estimation is provided in the supplementary material.

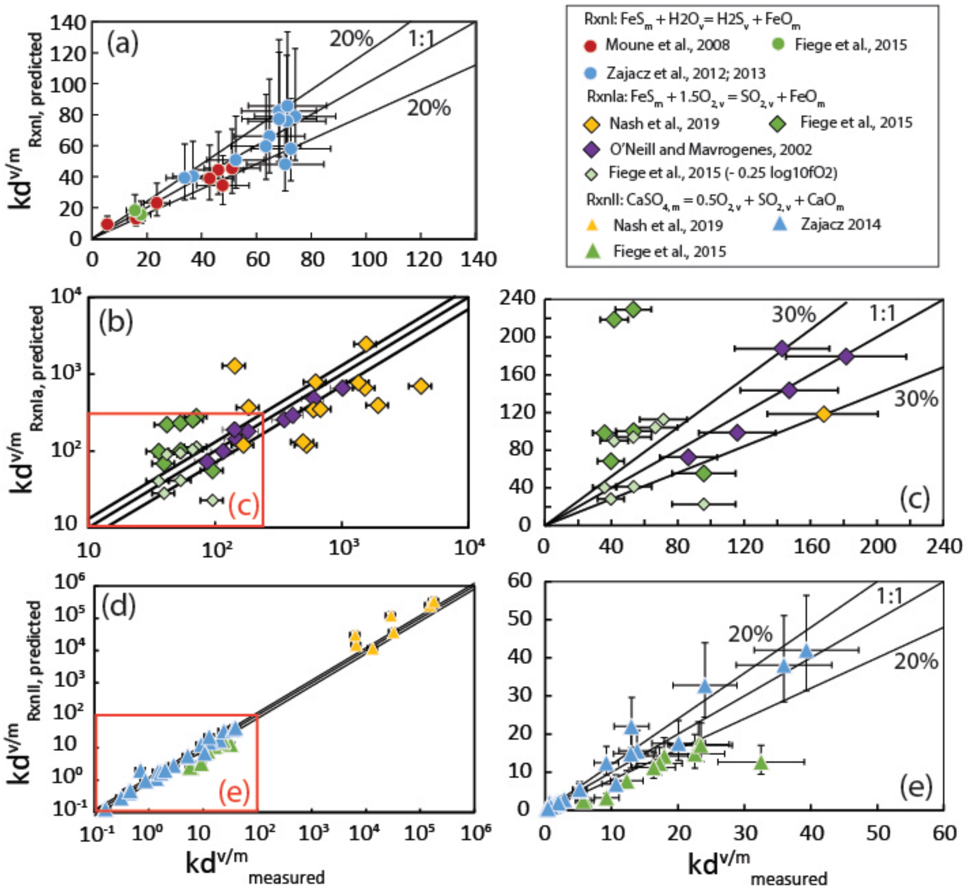

Figure 4. Comparisons between the measured $k_d(S)^{fl/m}$and the predicted $k_d(S)^{fl/m}$for RxnI (a), RxnIa (b, c) and RxnII (d, e). The error bars of the measured partition coefficients are assigned 20% for RxnI and RxnII, 30% for RxnIa. The error bars of the predicted partition coefficients are from the inverse regression, considering errors introduced from the experimental partition coefficients, the estimates of fO_2, and the major element concentration measured by electron probe.

3.3 The Sulfur_X Model: Combining partition coefficients with COH degassing and tracking of redox changes

The Sulfur_X model developed here is written as python scripts (Supplementary materials, also available on Github: https://github.com/sdecho/Sulfur_X.git). It takes the new $k_dS^{v/m}$ expressions (above) and combines them with (1) an existing COH degassing model (2) mass balance of components, (3) electron balance during Fe and S redox changes, and (4) equilibrium between oxidized and reduced Fe and S in the melt and S in the vapor to describe magma and gas evolution during ascent. To predict the COHS evolution in the melt and co-existing vapor during magma ascent, we took the approach of coupling an existing COH degassing model with sulfur partition coefficients ($k_d(S)^{v/m}$). However, instead of using the $k_d(S)^{v/m}$ tailored to a single volcanic system (Sisson and Layne, 1993; Burton et al., 2007; Johnson et al., 2010; Witham et al., 2012; Gennaro et al., 2020; Rasmussen et al., 2020), we employed the newly developed $kdS^{v/m}_{RxnI}$, $kdS^{v/m}_{RxnII}$, and $kdS^{v/m}_{RxnIa}$ to include the effects of changing P, T, H_2O, melt composition, fO_2, and sulfur speciation during magma ascent. This model assumes that all the gaseous species are in equilibrium with their counterparts dissolved in the melt. Only isothermal, closed-system degassing is considered at the current stage.

Figure 5 is a flowchart illustrating the structure of this model. The inputs to the model are the initial melt major element composition, concentrations of H_2O_0, $CO_{2,0}$, S_0, initial fO_2 relative FMQ buffer, and the initial temperature (Figure 5a). The outputs of the model are $kdS^{v/m}_{RxnI}$, $kdS^{v/m}_{RxnII}$, $kdS^{v/m}_{RxnIa}$. $kdS^{v/m}_{RxnI}$, $kdS^{v/m}_{RxnII}$, and $kdS^{v/m}_{combined}$, $Fe^{3+}/\Sigma Fe$, $S^{6+}/\Sigma S$, volatile composition of the melt (in wt.%) and the coexisting vapor (on both mol% and fugacity), as well as mass fractions of melt, vapor and crystals (if crystallization is enabled) of each degassing step. The model can be run with or without crystallization. If crystallization is enabled, then the major elements variations need to be specified as a function of the degree of crystallization, unless the default Fuego 1974 eruption is chosen. In the case of Fuego, the degree of crystallization (as indexed to K_2O concentration) changes as H_2O degasses, following the empirical relation constrained by Lloyd et al. (2013). The initial degassing pressure is calculated using H_2O_0 and $CO_{2,0}$ and an existing COH degassing model (the user can choose COH models from either Iacono-Marziano et al., 2012 or Newman and Lowenstern, 2002, Figure 5b). The pressure drops incrementally from the initial pressure to 1 atm, during which S degassing is calculated from sulfur partition coefficients between fluid and melt, and CO_2-H_2O degassing is calculated with the chosen COH degassing model as above and using mass balance at each degassing step. Since there are no experimental constraints for sulfur partition coefficients between 25 MPa and 1 atm, larger uncertainties are naturally involved in the predicted partition coefficients within this low-pressure range, which can cause large fluctuations in the predicted S contents as well as fO_2 evolution. Therefore, if needed to stabilize the model run at the low pressure range (25 MPa-1 atm), instead of using the calculated $kdS_{combined}^{v/m}$, Sulfur_X provides the option of increasing the $kdS_{combined}^{v/m}$ by a fixed number at each degassing step once the pressure drops below a certain threshold pressure (< 25 MPa). Both the fixed increase of the $kdS_{combined}^{v/m}$ and the threshold pressure can be changed by the user (more in the supplementary material).

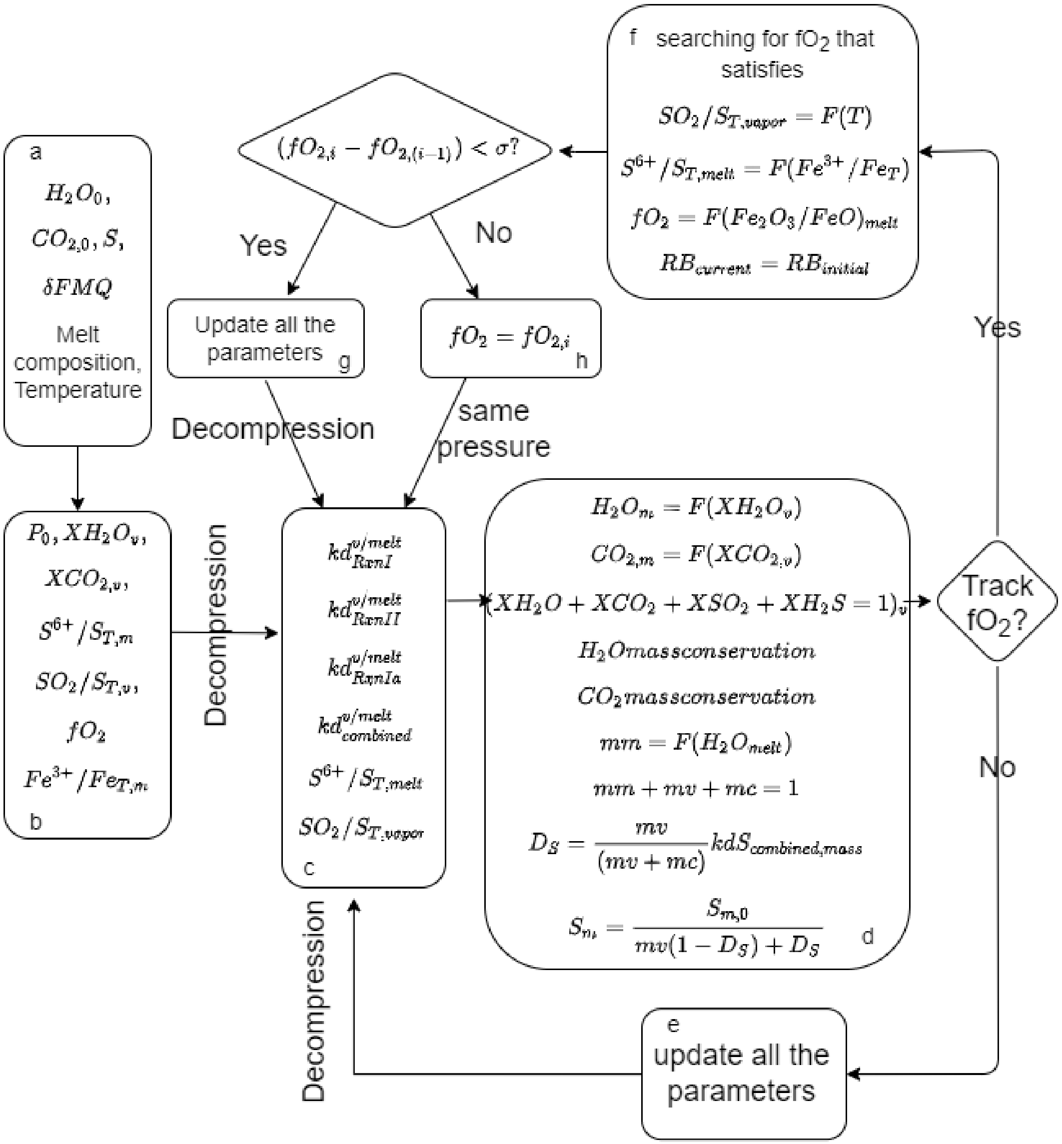

Figure 5. Flow chart of the degassing model. Operations of each box are detailed in the main text. All the required inputs of Sulfur-X are listed in panel a when all the outputs are listed in panel (c) and (d).

Without considering the redox state changes due to sulfur degassing, *fO_2* relative to FMQ buffer would remain unchanged through the entire degassing path. Instead, absolute *fO_2* and $Fe^{3+}/\Sigma Fe$ are dependent on decompression and is recalculated as a function of pressure, temperature, and melt composition (Kress and Carmichael, 1991) at every degassing step. At each degassing step, $SO_2/\Sigma S$ in the vapor is calculated with the *fO_2* at each current step, the *fH_2O*

from previous degassing step and the gas equilibrium equation (2). $kdS_{RxnI}^{v/m}$, $kdS_{RxnII}^{v/m}$, and $kdS_{RxnIa}^{v/m}$ are computed using the fH_2O, melt compositions, and sulfur speciation in the melt from the previous degassing step and fO_2 and $SO_2/\Sigma S$ in the vapor at the current step (Figure 5c). The pressure interval between each step can be specified by changing the number of steps, however, the interval needs to be small enough that changes in fH_2O, melt composition, and sulfur speciation in the melt are very small between steps. $kdS_{RxnI}^{v/m}$, $kdS_{RxnII}^{v/m}$, and $kdS_{RxnIa}^{v/m}$ describe S^{2-} in the melt degassing to H_2S in the vapor, S^{2-} to SO_2, and S^{6+} to SO_2, respectively. Figure 3a shows that these three degassing equilibria are likely to all be important within the transitional fO_2 range (e.g., FMQ to FMQ+2, Fig. 3), and it is not straightforward to constrain the contribution of each reaction to total sulfur degassing in an empirical model. Therefore, we implemented $kdS_{RxnI}^{v/m}$, $kdS_{RxnII}^{v/m}$, and $kdS_{RxnIa}^{v/m}$ in the degassing model by calculating an empirical $kd_{combined}^{v/m}$ weighted by the S speciation in the melt and in the vapor, as follows:

$$kd_{combined}^{v/m} = \left(\frac{S^{2-}}{S_t}\right)_{melt}\left(\frac{H_2S}{S_t}_{vapor} \times kdS_{RxnI}^{v/m} + \frac{SO_2}{S_t}_{vapor} \times kdS_{RxnIa}^{v/m}\right) + \left(\frac{S^{6+}}{S_t}\right)_{melt} \times kdS_{RxnII}^{v/m} \qquad (14)$$

With $kd_{combined}^{v/m}$ and the S concentration in the melt from the previous degassing step, total S content, fSO_2, and fH_2S in the vapor can be calculated. Although this approach using $kd_{combined}^{v/m}$ is highly empirical, we show below that it successfully reproduces natural data for melt inclusions and submarine glasses. CO_2 and H_2O concentrations in the melt are a function of the fCO_2 and fH_2O or partial pressure of CO_2 and H_2O in the co-existing vapor (Iacono-Marziano et al., 2012, equation (15, 16); Newman and Lowenstern, 2002), and the mass of CO_2 (Equation 17) and H_2O (Equation 18) in the system are conserved during equilibrium degassing. In addition, partial pressures of four volatiles (CO_2, H_2O, SO_2, H_2S) must sum to the total pressure at the current step (Equation 19). This means that the total pressure calculated by Sulfur_X at any step is larger than the total pressure calculated by the COH degassing models for the equivalent dissolved H_2O and CO_2 concentrations. If crystallization due to H_2O loss is considered, an empirical linear relation can be used to link the mass fraction of residual melt and the H_2O concentration in the melt (Lloyd et al., 2013, Equation 20). Lastly, the mass fractions of melt, vapor ± crystals must sum to 1 (Equation 21) for closed-system degassing. Solving Equations 15-21 together gives the concentrations of H_2O and CO_2 in the melt and vapor, mass fractions of melt (*mm*) and vapor (*mv*), and crystals (*mc*) if crystallization is enabled (Figure 5d).

$$\ln\left(CO2_{melt}^{ppm}\right) = \sum d_i x_i + aln\left(XCO2_{vapor} * P\right) + b + NBO + \frac{A}{T} + B + C * P/T \tag{15}$$

$$ln\left(H2O_{melt}^{wt.\%}\right) = \sum d_i x_i + aln\left(XH2O_{vapor} * P\right) + b + NBO + \frac{A}{T} + B + C * P/T \tag{16}$$

$$CO2_{melt}^{ppm} * mm + CO2_{vapor}^{ppm} * mf = CO2_{initial}^{ppm} \tag{17}$$

$$H2O_{melt}^{wt.\%} * mm + H2O_{vapor}^{wt.\%} * mf = H2O_{initial}^{wt.\%} \tag{18}$$

$$XSO2_{vapor} + XH2S_{vapor} + XH2O_{vapor} + XCO2_{vapor} = 1 \tag{19}$$

$$mm = F\left(H2O_{melt}^{wt.\%}\right) \tag{20}$$

$$mm + mv + mc = 1 \tag{21}$$

With the knowledge of the vapor and crystal fraction and the $kd_{combined}^{v/m}$, we calculate the bulk partition coefficient of sulfur between the non-melt phase and melt ($DS_{bulk}^{(v+crystal)/m}$). Lastly, sulfur concentration in the melt can be calculated using the initial S concentration, bulk S partition coefficient, and mass fraction of the melt (Figure 5d). Without considering redox state changes due to degassing (if redox evolution is disabled), the degassing calculation is finished after updating the CO_2, H_2O, and S concentration in the melt and the fluid, and mass fractions of melt, fluid, and crystals (Figure 5e). Then, the model decompresses to the next pressure step (Figure 5e-Figure 5c).

However, as S degasses from S^{2-} in the melt to H_2S and/or SO_2 in the vapor, and from S^{6+} in the melt to SO_2 in the vapor, electrons must exchange among different sulfur species and Fe^{3+}

and Fe^{2+} in the melt. Other gas species, like CO_2, H_2O, CO, CSO, and H_2 degassing could also have caused electron exchange. However, only trace amounts of H_2, CO, and CSO exist in the vapor of arc volcanic systems, and the impacts of these species on the redox state of the system are minor. Therefore, Sulfur_X only considers the redox exchange between S and Fe in the melt and H_2S and SO_2 in the vapor. The model tracks the redox evolution due to sulfur degassing by iteratively searching for a value of fO_2 that satisfies the S and Fe speciation in the melt and S speciation in the vapor after solving for COHS degassing described above.

The target fO_2 must satisfy four conditions (Figure 5f). First, the equilibrium between $SO_2/\Sigma S$ and fO_2 in the vapor (Equation 2) as a function of temperature (Equation 3) and pressure (through the use of fugacity coefficients) should be satisfied. Second, the equilibrium between fO_2 and $Fe^{3+}/\Sigma Fe$ in the melt (equation 18) from Kress and Carmichael (1991) should also be reached.

$$\ln\left(\frac{XFe_2O_3}{XFeO}_{melt}\right) = a\ln fO2 + \frac{b}{T} + C + \sum d_i x_i + e\left[1 - \frac{T0}{T} - \ln\left(\frac{T}{T0}\right)\right] + \frac{fP}{T} + g\left(\frac{T-T0}{T}\right)P + h\frac{P^2}{T} \quad (18)$$

Third, the calculated $Fe^{3+}/\Sigma Fe$ should be in equilibrium with $S^{6+}/\Sigma S$ in the melt (Equation 1), constrained using a relationship such as those proposed by Jugo (2010), Nash et al. (2019), O'Neill (2021) or Muth and Wallace (2021) at the given temperature. However, as discussed in section 2.1, it is still unclear whether the relatively large temperature effect proposed by Nash et al. (2019) is accurate, or whether other factors, such as melt composition, water content and pressure affect sulfur speciation in the silicate melt. In the case studies for Fuego and Hawaii discussed below, we followed the approach of Muth and Wallace (2021) in adopting the smaller temperature dependence of O'Neill (2021) and adjusted the equation to fit the S and Fe speciation measured by other studies for the specific systems of interest (Supplementary Fig. 4). For the users to apply the degassing model to other volcanic systems, the S-Fe redox relation is one of the free parameters that can be adjusted depending on the volcanic systems of interest (more details in the supplementary materials).

The last constraint comes from the conservation of the redox budget between Fe and S in the system. Redox budget is defined by Evans (2006) as the number of moles of negative charge that must be added to a sample to reach a reference state:

$$RB = \sum n_i v_i$$

where RB is the redox budget, n_i is the number of moles of an element with a certain valence state, and ν_i is the number of electrons required to take one mole of this element to the reference redox state. For example, RB of a system with 2 moles of Fe^{2+} and 1 mole of Fe^{3+} and with Fe^{3+} as the reference redox state is *RB* = 2 mole * (-1 electron) = -2 mole. Only Fe and S contribute to the redox budget in our degassing model, and Fe^{3+} and S^{6+} are the reference states. While electrons are exchanged among S^{6+}, S^{2-}, Fe^{3+}, Fe^{2+}, SO_2, and H_2S in the melt, vapor, and potentially crystals, redox budget of the system of melt, vapor with/without crystals is conserved along the degassing path. Currently, the Sulfur_X model assumes that crystallization does not change the $Fe^{3+}/\Sigma Fe$ ratio in the melt. But this can be easily modified if information on the crystals is available. Considering the conservation of the *RB* together with equations (2), (3), and (18), the degassing model solves for $S^{6+}/\Sigma S_{,\,melt}$, $Fe^{3+}/\Sigma Fe_{melt}$, $SO_2/\Sigma S_{vapor}$, and fO_2. With the updated fO_2 (Figure 5h), at the same pressure, the model repeatedly solves for sulfur partition coefficients, COHS degassing, and fO_2 until the fO_2 stops changing within a certain error (Figure 5c, 5d, 5f, 5h). Then, the model updates all the parameters and decompresses to the next pressure step (Figure 5g-Figure 5c). When solving for fO_2, it is possible that there are outlier results during degassing, especially at low pressure when $kd^{v/m}_{combined}$ can be large. These outliers can be minimized by choosing the appropriate model parameters (details in the supplementary material).

4. APPLICATION OF SULFUR_X TO MAGMA DEGASSING

We tested Sulfur_X against the empirical degassing trends described by melts from Fuego and from Kilauea and Mauna Kea volcanoes, Hawaii. For Fuego, we used experimentally rehomogenized melt inclusions from the 1974 eruption (Rasmussen et al., 2020). The CO_2 concentrations and the degassing depths of this dataset have been reconstructed by rehomogenization experiments, and they display a co-degassing trend of S and CO_2 (Figure 1). These data make a good test case for the new sulfur partition coefficients, particularly their extrapolation to high pressure. We also tested the model against melt inclusions from Kilauea volcano (Moussallam et al., 2016) and submarine glasses from Mauna Kea volcano (Brounce et al., 2017). The $Fe^{3+}/\Sigma Fe$ in the Kilauea melt inclusions and the $S^{6+}/\Sigma S$ and $Fe^{3+}/\Sigma Fe$ in the Mauna Kea glasses were measured by XANES and are used to test the model predictions of the redox evolution due to sulfur degassing.

4.1 Magma degassing at Fuego and comparison to other models

For the Fuego 1974 magma degassing model, the initial volatile concentrations are taken from the highest measured in the melt inclusion population (Rasmussen et al., 2020), 4.5 wt.% H_2O, 2650 ppm S, and 3300 ppm CO_2 (reconstructed). Lloyd et al., (2013) used V partitioning between the Fuego MIs and their corresponding host olivines to estimate the fO_2 between FMQ+1.2 for the more mafic phenocrysts (Fo77–78) and FMQ+0.76 for Fo73–74 phenocrysts. Thus, the initial $Fe^{3+}/\Sigma Fe$ in the melt was chosen as 0.23, corresponding to FMQ+1.2 at the initial *P-T* conditions. The model is run isothermally at the temperature of 1030℃ (Lloyd et al., 2013). With the initial $Fe^{3+}/\Sigma Fe$ calculated by the initial fO_2 value (FMQ+1.2) and temperature, the initial $S^{6+}/\Sigma S$ in the melt is ~0.7, calculated by the modified S speciation model from Muth and Wallace (2021). We modified the last constant in the Muth and Wallace model (which uses the O'Neill, 2021, temperature dependence) to match the $S^{6+}/\Sigma S$ vs. $Fe^{3+}/\Sigma Fe$ curve defined by the experimental data from Jugo et al. (2010) for a basaltic composition and temperature (1050℃) similar to Fuego magma (Supplementary Fig.4). Previous studies show that the Fuego melt compositions changed during degassing, from SiO_2 of 48 to 58 wt.%. as S decreased from 2650 to 500 ppm (Lloyd et al., 2013; Rasmussen et al., 2020). Therefore, the model includes crystallization, controlled by the empirical relation between H_2O and K_2O concentration (Lloyd et al., 2013) and assuming K_2O is perfectly incompatible. The evolution of other major elements along the degassing and crystallization trend is empirically parameterized as a function of the degree of crystallization (Lloyd et al., 2013; Rasmussen et al., 2020). We employed the COH degassing model from (Iacono-Marziano et al., 2012) that includes melt composition as parameters. For low-pressure degassing, the model run is stable if $kd_{combined}^{v/m}$ increases by 20 at each degassing step when pressure decreases below 15 MPa (the last 8 steps). If a user is not interested in the lowest pressure stage of degassing, we recommend specifying a final pressure of 25 MPa or higher (more details in the supplementary material).

Figure 6 compares the rehomogenized (Rasmussen et al., 2020) and untreated (Lloyd et al., 2013) Fuego MIs to the degassing results for S-CO_2 (Fig. 6a) and S-H_2O (Fig. 6b) from Sulfur_X. Model 1 (solid blue curve in Fig. 6a) represents the results from the initial conditions described above. The error envelope derives from a Monte Carlo scheme, where the degassing model was run 100 times, with each run employing random numbers generated within 1σ of the predicted $kdS_{RxnI}^{v/m}$, $kdS_{RxnII}^{v/m}$, and $kdS_{RxnIa}^{v/m}$. The light blue shading represents the standard deviation of 100 modeled runs. Model 1 predicted a co-degassing trend of S and CO_2 close to the MI data. However, compared to the Fugeo rehomogenized MIs, it predicts higher sulfur at given CO_2 concentrations. One potential explanation for the mismatch is that the initial CO_2

concentration from the undegassed parental magma is higher than the highest CO_2 concentration from the rehomogenized experiments. Given that only two rehomogenized melt inclusions with CO_2 higher than 2000 ppm define the early degassing path, the initial CO_2 from the undegassed parental magmas may be higher than 3300 ppm. For example, Model 2 (yellow solid curve in Fig. 6) starts with 5000 ppm CO_2, and the predicted CO_2-S trend in the melt better fits the rehomogenized MIs.

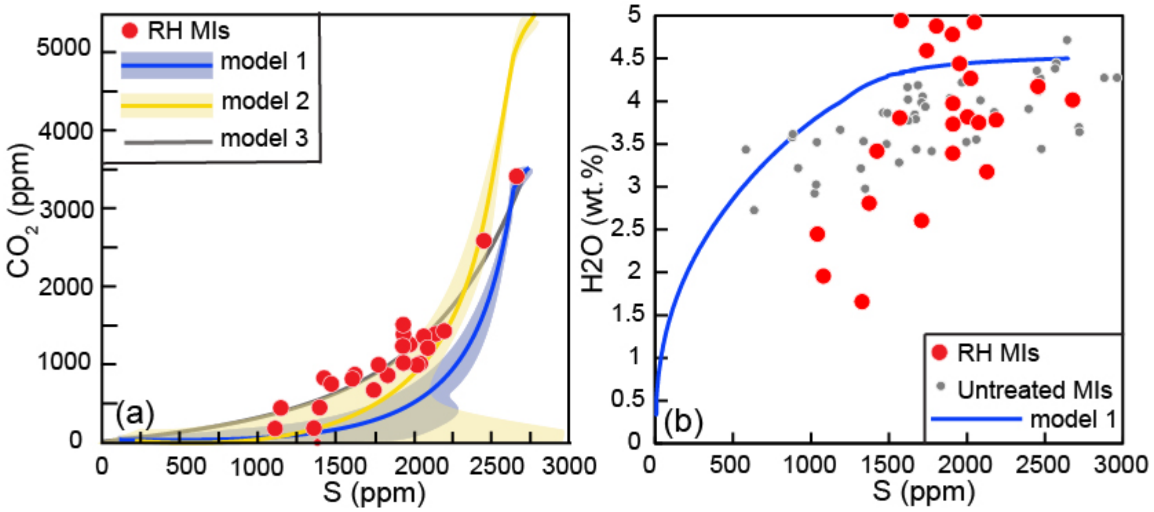

Figure 6. (a) Comparison of CO_2-S concentration between the rehomogenized Fuego MIs (Rasmussen et al., 2020) and the Sulfur_X modeled degassing with 3300 ppm CO_2 (model 1), 5000 ppm CO_2 (model 2), and 3300 ppm CO_2 + 0.25 wt.% sulfide crystallization (model 3). (b) Comparison of H_2O-S concentration between the rehomogenized (Rasmussen et al., 2020) and untreated melt inclusions (Lloyd et al., 2013) and the Sulfur-X model results with 3300 ppm initial CO_2 (model 1). Modeling details are described in the main text.

Figure 6. (a) Comparison of CO_2-S concentration between the rehomogenized Fuego MIs (Rasmussen et al., 2020) and the Sulfur_X modeled degassing with 3300 ppm CO_2 (model 1), 5000 ppm CO_2 (model 2), and 3300 ppm CO_2 + 0.25 wt.% sulfide crystallization (model 3). (b) Comparison of H_2O-S concentration between the rehomogenized (Rasmussen et al., 2020) and untreated melt inclusions (Lloyd et al., 2013) and the Sulfur-X model results with 3300 ppm initial CO_2 (model 1). Modeling details are described in the main text.

Another potential factor causing the mismatch between the results from Model 1 and the rehomogenized MIs is sulfide saturation. Sulfide inclusions inside the melt inclusions, magnetite, and olivine have been observed in products of the 1974 eruption (Rose et al., 1978; Lloyd et al., 2013). Model 3 (solid grey curve in Fig. 6a) demonstrates that without changing the initial CO_2 concentration, 2 wt.% sulfides in the crystallizing assemblage throughout the differentiation can sequester enough sulfur from the melt to match the S concentration in the rehomogenized MIs, especially at the high CO_2 stage. However, 2 wt.% sulfide in the crystals has non-negligible effects on the concentration of chalcophile elements, like Cu (Supplementary Fig. 5) and Ag, and the model does not match the K_2O-Cu whole rock data of the 1974 eruption (Lloyd et al., 2013). Therefore, Model 3, where the Fuego magma was sulfide saturated from an early stage, can be excluded. Fig. 6b shows the modeled S-H_2O degassing trend from Model 1, very similar to the results from Model 2 with higher initial CO_2 concentrations. The modeled result demonstrates that significant S degases (> 1000 ppm) before H_2O degasses (< 0.5 wt.%), which is consistent with the untreated melt inclusion data from Fuego 1974 eruption (Lloyd et al., 2013). The rehomogenized melt inclusions show a steeper H_2O decrease as S decreases, however, H_2O concentration in the rehomogenized melt inclusions could be compromised during rehomogenization experiments (Rasmussen et al., 2020)

4.1.1 Change in each kd and sulfur speciation as a function of pressure.

Although the Sulfur_X degassing model describes a CO_2-S path that approximates that defined by the homogenized melt inclusions from Fuego (Fig. 6), this result is the sum of complex variations in the $k_dS^{v/m}$ values and sulfur species as a function of pressure. Here we explore the variation of each of the individual $k_dS^{v/m}$ values, and how each contributes to the behavior of bulk sulfur in the melt. Both $kdS_{RxnII}^{v/m}$ and $kdS_{RxnIa}^{v/m}$ increase significantly as pressure decreases whereas $kdS_{RxnI}^{v/m}$ increases slightly with decreasing pressure to 200 MPa then slightly decreases as pressure continues dropping. The significant negative effects of pressure on all partition coefficients come from the -lnP term in equations (11-13). However, such a negative

P effect is counteracted by decreasing fH_2O (Figure 7e), which results in decreasing $kdS_{RxnI}^{v/m}$ at pressure lower than 200 MPa. At pressure below 200 MPa, the increase of $kdS_{RxnIa}^{v/m}$significantly slows down when $kdS_{RxnII}^{v/m}$ continues increasing by orders of magnitudes. The decoupling of $kdS_{RxnIa}^{v/m}$ and $kdS_{RxnII}^{v/m}$ as pressure decreases is likely due to the decreasing fO_2 (Figure 7d) that increases $kdS_{RxnII}^{v/m}$ (equation 6) and decreases $kdS_{RxnIa}^{v/m}$ (equation 5).

Next, we consider how each partition coefficient contributes to $kdS_{combined}^{v/m}$, based on the sulfur speciation in the melt and vapor. The S speciation in the melt is closely linked to the Fe speciation. $Fe^{3+}/\Sigma Fe$ varies little between 600-400 MPa, increases to 0.29 as pressure decreases to 75 MPa, and then decreases rapidly as pressure continues dropping. The $Fe^{3+}/\Sigma Fe$ change with pressure translates to $S^{6+}/\Sigma S$ (Figure 7c) and ΔFMQ (Figure7d) showing similar increasing then decreasing trends. In contrast, SO_2/S_T in the vapor first decreases slightly from ~0.55 to ~0.4 due to the decreasing absolute fO_2 as pressure decreases to ~400 MPa while maintaining almost constant $Fe^{3+}/\Sigma Fe$ ratios. Then SO_2/S_T increases up to 0.9 as pressure decreases to the surface, likely due to the decreasing f_{H_2O} (Figure 7e) and the changing fO_2. $kdS_{combined}^{v/m}$ is calculated using $kdS_{RxnI}^{v/m}, kdS_{RxnIa}^{v/m}, and\ kdS_{RxnII}^{v/m}$, with each reaction weighted by S speciation in the melt and in the vapor (equation 14). Because the $S^{6+}/\Sigma S$ of the melt is always > 0.7, the combined kd is always dominated by RxnII. At pressures lower than 100 MPa, the predicted $kdS_{combined}^{v/m}$ increases rapidly to ~2000 at 1 atm, almost overlapping with $kdS_{RxnII}^{v/m}$. The extremely high $kdS_{combined}^{v/m}$ at low pressures is mainly due to rapid increase of $kdS_{RnxII}^{v/m}$, resulting from decreasing pressure and fO_2.

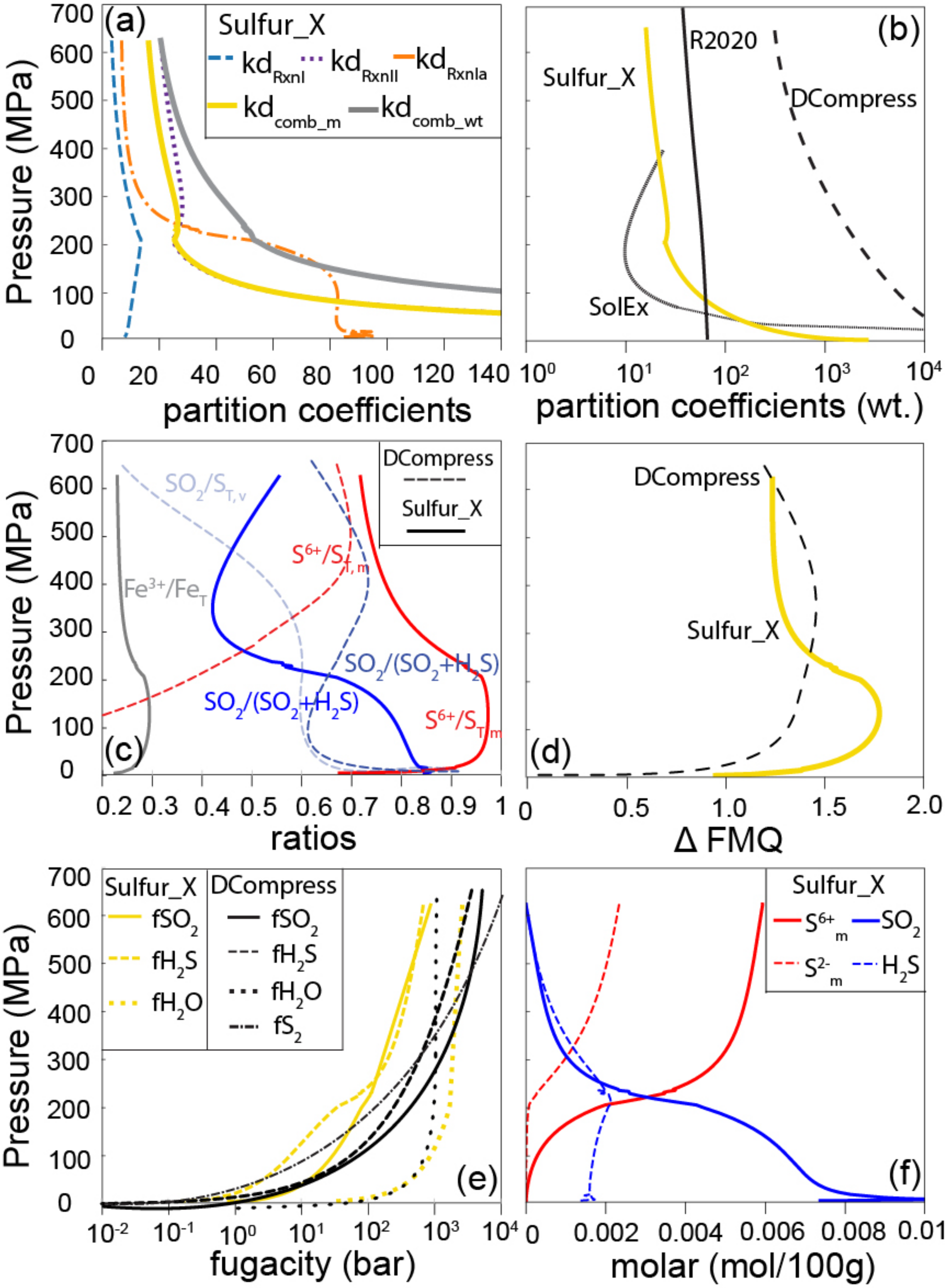

Figure 7. More model results for Fuego with 5000 ppm initial CO_2, and comparison to previous models, empirical fit (Rasmussen et al., 2020), SolEx (Witham et al., 2012), and D-Compress (Burgisser et al., 2015). All parameters are plotted against degassing pressure. (a) Modeled sulfur partition coefficients with all kd's in molar units, except for the combined sulfur partition coefficient (in wt% as well, yellow solid curve). (b) Comparisons of apparent sulfur partition

coefficients in wt.% from this study (solid yellow curve), empirical fit (solid black curve), SolEx(dotted curve), and D-Compress (long dashed curve). Apparent sulfur partition coefficients from the previous models are recalculated with $S_{vapor,\ wt.\%}/S_{melt,\ wt.\%}$ from their model results. (c) Comparison of calculated S^{6+}/S_T in the melt (red cuves) and $SO_2/(SO_2+H_2S)$ in the vapor (dark blue curves) from this study (solid curves) and D-Compress (long dashed curves). SO_2/S_T (where $S_T = SO_2+H_2S+S_2$ in moles) from D-Compress is also plotted (light blue long dashed curve). Fe^{3+}/Fe_T in the melt from this study is also shown (solid grey curve). (d) Comparisons between the *fO_2* relative to FMQ buffer predicted by this study (yellow solid curve) and D-Compress (long dashed curve). (e)Comparison of SO_2 (solid), H_2S (dashed) and H_2O (dotted) fugacity predicted by this study (yellow) and D-Compress (black). S_2 fugacity predicted by D-Compress is also plotted (black dash-dot curve). (f) Moles of S^{6+}(red solid curve), S^{2-}(red dashed curve), SO_2 (blue solid curve), and H_2S (blue dashed curve) change during degassing modeled by this study, calculated with 100g total weight of the system.

Although the above analysis explains the dominant factors that contribute to $kdS^{v/m}_{combined}$, it is challenging to tease apart the drivers and responses of S and Fe speciation and fO_2, which are inextricably linked via electron exchange. Sulfur_X captures not only the effect of evolving *fO_2* on S degassing but also the electron exchange between Fe and S as a consequence of degassing, depending on the contribution of the three degassing reactions. For example, S^{2-} degassing to H_2S (RxnI) does not cause any electron exchange. During RxnII, one mole of S^{6+} degasses to $S^{4+}O_2$ by receiving 2 moles of electrons, likely donated by the Fe^{2+}. Therefore, S^{6+} degassing to SO_2 (RxnII) increases $Fe^{3+}/\Sigma Fe$. In contrast, during RxnIa, $Fe^{3+}/\Sigma Fe$ decreases when Fe^{3+} receives 6 moles of electrons from S^{2-} when 1 mole of S^{2-} degasses to 1 mole of $S^{4+}O_2$. In Fuego's case, each reaction's contribution can be best visualized if we consider the molar change of S^{6+}, S^{2-}, SO_2, and H_2S in a system of 100 g total weight (Figure 7f). At pressures higher than 200 MPa, the increase in moles of H_2S and SO_2 in the vapor phase is almost mirrored by the decrease of S^{2-} and S^{6+}in the melt, suggesting that RxnI and RxnII are the dominant degassing reactions at this stage. As a result of RxnII, $Fe^{3+}/\Sigma Fe$ increases. This oxidizing effect becomes pronounced as the fraction of vapor phase increases, also as the fraction of S^{6+} in the melt increases, responding to the increase of $Fe^{3+}/\Sigma Fe$. Therefore, $kdS^{v/m}_{RxnII}$ becomes increasingly dominant in the $kdS^{v/m}_{combined}$. Meanwhile, also responding to the increased $Fe^{3+}/\Sigma Fe$, SO_2/S_T in the vapor increases rapidly, which eventually requires S^{2-} degassing to SO_2 (RxnIa). The occurrence of RxnIa is suggested in Figure 7f when the consumption of S^{2-} outweighs the increase of H_2S between 300 and 200 MPa. In contrast to RxnII, RxnIa has a strong reducing impact from donating 6 moles of electrons to Fe^{3+} as every mole of S^{2-} degasses. Therefore, RxnIa slows down the increase of $Fe^{3+}/\Sigma Fe$ between 300 and 100 MPa until S^{2-} is almost fully consumed. Around 200 MPa, another interesting change is the decrease in the amount of H_2S when both S^{2-} and S^{6+} continue decreasing (Fig. 7f). The decrease of H_2S accompanies the significant increase in SO_2 in the vapor that outweighs the decrease of S^{6+} in the melt. Since it is a closed system, H_2S in the vapor can only be converted to SO_2 to satisfy the gas equilibrium (equation 2). The redox change from H_2S to SO_2 in the vapor can efficiently reduce $Fe^{3+}/\Sigma Fe$ in the melt. Therefore, the modeled $Fe^{3+}/\Sigma Fe$ change is the net effect of donating electrons as S^{6+} in the melt degasses to SO_2 (RxnII), receiving electrons as S^{2-} degasses to SO2 (RxnIa) and through H_2S conversion to SO_2 in the vapor. The reduction efficiency of the H_2S-SO_2 gas equilibrium and the trace amount of S^{2-} degassing to SO_2 outweigh the oxidizing efficiency of RxnII, and result in the rapid reduction of $Fe^{3+}/\Sigma Fe$ during the last stage of degassing (< 100 MPa).

4.1.2 Comparison to other degassing models

Figure 7b compares the computed $kdS^{v/m}_{combined}$ from Sulfur_X to that for three other degassing models: SolEx, D-Compress, and the empirical fit of Rasmussen et al. (2020). Since these models employ different approaches to model sulfur degassing, we recalculated the apparent $kdS^{v/m}(C_{S,vapor}/C_{S,melt})$ using the modeled sulfur concentration in the vapor and in the melt to compare different models. The predicted $kdS^{v/m}_{combined}$ from Sulfur_X varies from 20 to 80 at pressures higher than 100 MPa, agreeing well with the partition coefficients (40-60) derived by the empirical model (Rasmussen et al., 2020). It is not surprising that the empirical fit does not capture the rapid increase of apparent $kdS^{v/m}$ during the last stage of degassing, since the empirical fit assumed a constant partition coefficient between melt and non-melt phases throughout the degassing process, and also because most melt inclusions were entrapped at pressures higher than 100 MPa. Although both the apparent $kdS^{v/m}$ from SolEx and D-Compress increase significantly at low pressure like Sulfur_X, they differ strongly at high pressure. For SolEx, the maximum initial pressure that can be used is 400 MPa, the highest experimental pressure of the calibration experiments (Lesne et al., 2011). Therefore, the model run starts with ~1100 ppm CO_2 and 2100 ppm S at 400 MPa. Between pressure of 400 and 100 MPa, the apparent $kdS^{v/m}$ from SolEx starts around 20 but rapidly decreases to <10, significantly lower than the $kdS^{v/m}_{combined}$ at the same pressure. This low apparent $kdS^{v/m}$ explains why SolEx predicts almost no sulfur degassing for Fuego until pressures lower than 100 MPa, when CO_2 is almost entirely degassed (Figure 1).

In contrast, the apparent $kdS^{v/m}$ from D-Compress appears to be at least one order of magnitude higher than the $kdS^{v/m}_{combined}$ from Sulfur_X and is responsible for the concave-up shape of the model CO_2-S degassing trend in Figure 1. It is important to note that D-Compress does not allow initial S concentration as a model input. Instead, fSO_2, fH_2S and fS_2 are calculated in the vapor based on the input of initial fO_2 (input as FMQ+1.2), initial H_2O (4.5 wt.%), and initial CO_2 (3300 ppm) in the system by gas equilibrium, fugacity laws and mass balance. The initial pressure is 650 MPa, and temperature 1030°C. Such starting inputs give S concentration of ~2700 ppm in the melt, very close to the initial conditions run by Sulfur_X. However, D-Compress calculates 46 mol% S_2 together with 18 mol% SO_2 and 11 mol% H_2S in the initial vapor. Figure 7e shows that for most of the degassing path (P> 50 MPa), fSO_2 and fH_2S predicted by D-Compress are almost an order of magnitude higher than those predicted by Sulfur_X. The predicted high fSO_2, fH_2S, and fS_2 make S the most abundant volatile species in the vapor until the pressure drops to < 300 MPa. Since the mass of S is conserved in the system, high sulfur contents in the vapor cause the rapid decrease of S in the melt and, thus, the high apparent $kdS^{v/m}$ shown in Figure 7b. The high total S in the vapor also results in low fH_2O (Figure 7e) at high pressure, due to dilution of H_2O in the vapor phase. D-Compress solves for fSO_2, fH_2S, fS_2 in the vapor together with the fugacities of the other six gas species at each pressure step (Burgisser et al., 2015), and it is unclear what factor(s) caused the unreasonably high fSO_2, fH_2S, and fS_2.

We can also compare the fO_2 and S speciation evolution between Sulfur_X and D-Compress. The predicted $SO_2/S_{T,v}$ from D-Compress increases dramatically as pressure decreases (Figure 7c), primarily due to the fast decrease of fS_2 in the vapor (Figure 7e). The predicted $S^{6+}/\Sigma S$ in the melt from D-Compress follows the changing $SO_2/(SO_2+H_2S)$ until 100 MPa. This is not surprising because D-Compress does not directly calculate the S speciation in the melt. Instead, it computes the concentration of S^{2-} and S^{6+} in the melt separately using fH_2S and fSO_2 and their solubility laws (Burgisser et al., 2015). Therefore, D-Compress only considers fO_2 change due to reactions between different volatile species in the vapor and reaction between fO_2, Fe^{3+}, and Fe^{2+} in the melt. It ignores the S redox change when S degasses from melt to the vapor and its potential effects on $Fe^{3+}/\Sigma Fe$. However, our model shows that fO_2 in the system might be dominated by different processes at different degassing stages. The gas equilibrium for S species in the vapor (H_2S converting to SO_2 for Fuego case) plays an important role at low pressure, where most S has already been degassed. RxnIa, S^{2-} degassing to SO_2, and RxnII, S^{6+}

degassing to SO_2, on the other hand, significantly affect $Fe^{3+}/\Sigma Fe$ in the melt, thus the fO_2, during high pressure degassing.

4.2 Magma degassing in Hawaiian volcanoes and comparison to arc magma degassing

We apply Sulfur_X to the degassing of H_2O-poor and more reduced magmas from Hawaii with lower initial ΔFMQ and lower initial $S^{6+}/\Sigma S$ ratio (~0.1). This experiment provides a contrast to our earlier example of an H_2O-rich, high initial $S^{6+}/\Sigma S$ ratio (~0.7) arc magma from Fuego. For the Hawaiian degassing model, the initial H_2O and S concentrations are taken from the highest concentrations measured in Kilauea melt inclusions (Moussallam et al., 2016) and Mauna Kea glasses (Brounce et al., 2017): 0.6 and 0.3 wt.% H_2O and 1500 and 1600 ppm S, respectively. CO_2 concentrations were not corrected for vapor bubbles in these studies. The initial CO_2 of the undegassed magma is assumed to be 4000 ppm, among the highest CO_2 concentration measured in Kilauea Iki melt inclusions after restoration using Raman spectroscopy and 1 atm reheating experiments (Moore et al., 2015; Tuohy et al., 2016). The initial fO_2 are FMQ+0.6 for Kilauea Iki and FMQ+0.8 for Mauna Kea lava, to match the measured $Fe^{3+}/\Sigma Fe$ ratios in the least degassed melt inclusion (0.19) or submarine glass (0.2). The model temperature is fixed at 1150℃. The measured $S^{6+}/\Sigma S$ associated with the least degassed sample from Mauna Kea (Brounce et al., 2017) is assumed for the initial $S^{6+}/\Sigma S$ in the melt (~0.1). Again, we modified the last constant of the Muth and Wallace model to match the measured $S^{6+}/\Sigma S$ and $Fe^{3+}/\Sigma Fe$ in the pillow rim glasses (Supplementary Fig. 4) from Mauna Kea (Brounce et al., 2017). Crystallization is disabled in this run, as the lower H_2O of Hawaiian magmas results in no decompression-driven crystallization until the very end of the degassing path. We employed the VolatileCalc degassing model (Newman and Lowenstern, 2002) for these low-H_2O magmas. To stabilize the model run in the low pressure range, after 8 MPa, instead of using the computed $kdS^{v/m}_{combined}$, we assumed that $kdS^{v/m}_{combined}$ increases by 50 at each degassing step until 1 atm (the last 4 steps).

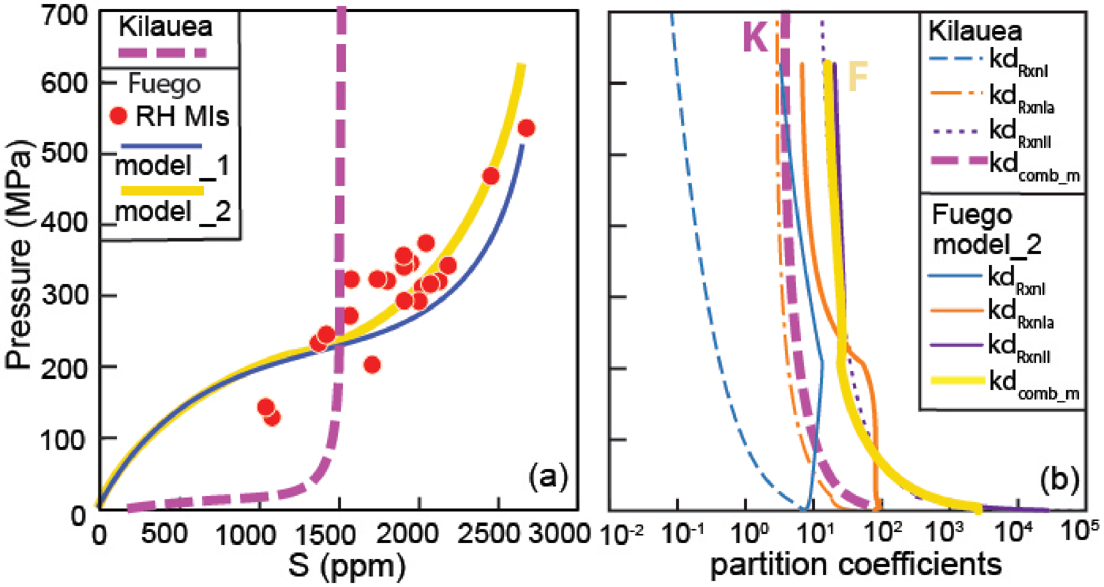

Figure 8. Comparison of model results for Kilauea magma, in comparison to Fuego model results. (a) Modeled S concentration change as a function of pressure for Kilauea (pink dashed), and Fuego (model 1 with 3300 ppm initial CO_2, dark blue solid curve; model 2 with 5000 ppm initial CO_2, yellow solid curve). S contents and pressure calculated by restored CO_2-H_2O concentration of rehomogenized Fuego melt inclusions (red symbols) are also plotted for comparison. (b) Sulfur partition coefficients for Kilauea of RxnI (blue dashed), RxnIa (orange dash-dot) and RxnII (purple dotted) and the combined partition coefficient in wt.% for Kilauea (thick pink dashed curve) are in comparison with sulfur partition coefficients predicted for Fuego (blue, orange, and purple thin solid curves for RxnI, RxnIa, and RxnII, and thick yellow solid curve for combined partition coefficient in wt.%) with 5000 ppm initial CO_2.

The model results are plotted in Figure 8 and Figure 9. One of the critical observations from the model results for Hawaiian magma is the S evolution in the melt as a function of pressure (exemplified by Kilauea in Figure 8a). In contrast to the prediction of Fuego magma that S degasses from 500 to 100 MPa, our degassing model predicts that S in the melt stays almost constant until pressure drops to below 100 MPa. 75% of the total S degassing occurs in the last 40 MPa during magma ascent. This predicted shallow degassing of S is consistent with the semi-empirical model results from Gerlach (1986) and Lerner et al. (2021) that both S and H_2O

degassing do not begin until the melts reach 100-200 m (2-5 MPa) beneath the surface. However, Sulfur_X predicts S degassing earlier than H_2O, which matches the S-H_2O trends (Fig. 9a) defined by the Kilauea melt inclusions (Moussallam et al., 2016) and Mauna Kea glasses (Brounce et al., 2017). The low-pressure (<40 MPa) sulfur degassing is a direct result of the $kdS^{v/m}_{combined}$, a weighted average of the $kdS^{v/m}_{RxnI}$, $kdS^{v/m}_{RxnII}$, $kdS^{v/m}_{RxnIa}$. Figure 8b shows that the calculated $kdS^{v/m}_{RxnI}$ and $kdS^{v/m}_{RxnIa}$ are between <0.1 to <10, and <10 to 100, respectively, until the pressure drops to below 100 MPa. They are 2 and 1 order of magnitude lower, respectively, than the $kdS^{v/m}_{RxnI}$ and $kdS^{v/m}_{RxnIa}$ for Fuego magma. Since both H_2O mole fraction in the melt and H_2O fugacity can enhance $kdS^{v/m}_{RxnI}$ and $kdS^{v/m}_{RxnIa}$, the ~ ten times lower H_2O concentration and five times lower H_2O fugacity of Kilauea magma likely causes the much lower predicted $kdS^{v/m}_{RxnI}$ and $kdS^{v/m}_{RxnIa}$ compared to Fuego magma at a given pressure. In contrast, $kdS^{v/m}_{RxnII}$, which is not directly affected by H_2O in the system, is very similar for Kilauea and Fuego magmas (Figure 8b). However, the Hawaii magma has a low initial $S^{6+}/\Sigma S$ of around 0.1 (Figure 9c, Brounce et al., 2017), and > 0.9 SO_2/S_T in the vapor because of high absolute fO_2, temperature, and low fH_2O (Figure 9b). As a result, $kdS^{v/m}_{RxnIa}$ dominates the $kdS^{v/m}_{combined}$ (Figure 8b). Since $kdS^{v/m}_{RxnIa}$ maintains low values (between 1 and 10) until the last 50 MPa, $kdS^{v/m}_{combined}$ and S degassing are low for Hawaiian magmas until shallow pressure. The dominance of RxnIa also explains the predicted continuous reduction of $Fe^{3+}/\Sigma Fe$ in the melt inclusions (Figure 9d): Fe^{3+} receives electrons from S^{2-} when S^{2-} degasses to $S^{4+}O2$. The reduction of Fe drives a decrease of fO_2, which increases the H_2S fraction in the vapor (Figure 9b) and requires more of RxnI's contribution. RxnIa remains the dominant reaction that affects the redox states of S and Fe in the system. The effect from RxnII appears to be very small given the small amount of S^{6+} in the melt and its low efficiency in transferring electrons compared to RxnIa. Therefore, $S^{6+}/\Sigma S$ and $Fe^{3+}/\Sigma Fe$ in Hawaii magmas continuously decrease, in contrast to the more complex behavior displayed by Fuego magma. As a result of decreasing fO_2 in Kilauea magma, SO_2/S_T in the vapor decreases from > 0.95 to ~ 0.5 (Figure 9b) and increases back to ~0.8 as water fugacity continues falling at low pressure. The predicted SO_2/S_T in the vapor at 1atm (~0.8), however, is slightly lower than that from the gas measurements at the surface (Figure 9b), which is between 0.9 and 1(Gerlach, 1986).

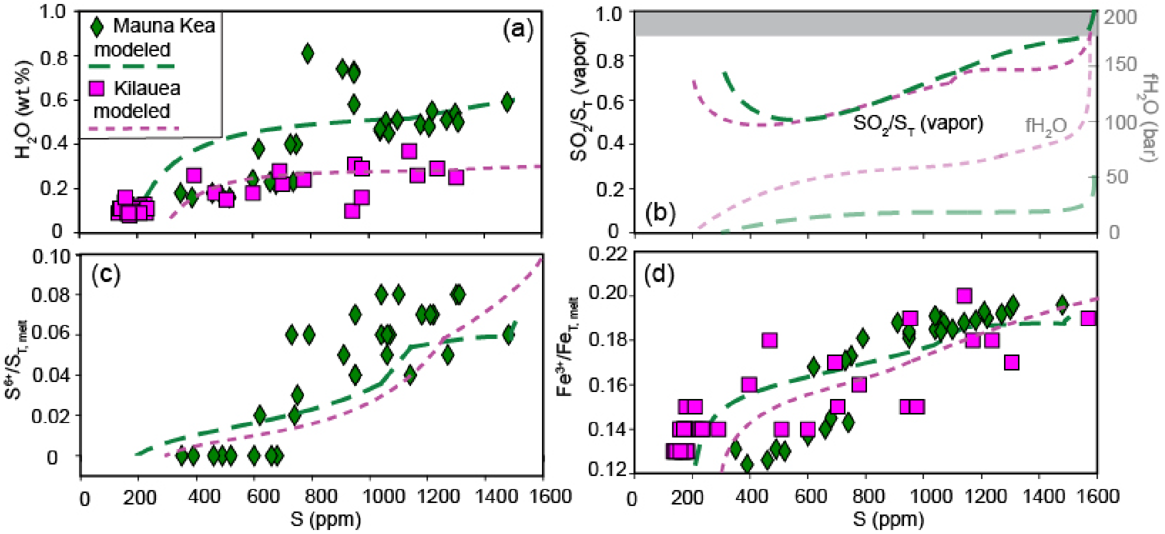

Figure 9. Comparisons of the measured (symbols) and modeled (dashed lines) S and Fe speciation changes during degassing for Kilauea (melt inclusion data from Moussallam et al., 2016) and Mauna Kea (pillow rim glasses data from Brounce et al., 2017). Grey bar in panel b shows the observed range of SO_2/S_T, 0.9-1, in the volcanic gases from Kilauea volcano (Gerlach, 1986)Modeling details are described in the main text.

It is important to note that although the initial fO_2 relative to FMQ buffer of Hawaiian magma is lower than that of Fuego, the equivalent absolute log fO_2 value calculated by the initial buffer, melt composition, pressure, and temperature, is around -7.5 (Kress and Carmichael, 1991), higher than that calculated for Fuego magma (~-8.7). Since both $kdS^{v/m}_{RxnIa}$and $kdS^{v/m}_{RxnII}$ depend on absolute fO_2 as an input, their values are not appreciably lower as might be expected for more reduced magma than Fuego. Therefore, we emphasize here that the key impact of initial *fO_2* on S degassing in Hawaiian magmas is through the low initial $S^{6+}/\Sigma S$ in the melt and the consequent reduction during degassing. Since it is still unclear from experimental data what the equilibrium relationship between $Fe^{3+}/\Sigma Fe$ and $S^{6+}/\Sigma S$ in the melt should be, we encourage users to define this relation with caution (more in supplementary material), as it can affect the model results significantly. Figure 9 also shows the comparison between the results of Sulfur-X and the H_2O, S, $S^{6+}/\Sigma S$, and $Fe^{3+}/\Sigma Fe$ measured in melt inclusions from Kilauea and submarine glasses from Mauna Kea (Brounce et al., 2017; Moussallam et al., 2017). Figure 9a shows that the modeled melt H_2O-S evolution for Kilauea and Mauna Kea passes through the melt inclusion and submarine glass data, respectively. Both data sets show significant S degassing (>50%) when little H_2O degasses (<0.1 wt.% H2O), which is inconsistent with the predictions from Gerlach (1986) and Lerner et al., (2021), that S only begins to degas when H_2O degasses significantly. Figure 9c and 9d show that the modeled $S^{6+}/\Sigma S$ and $Fe^{3+}/\Sigma Fe$ decrease as S degasses, similar to that measured in the Mauna Kea glasses. The modeled $Fe^{3+}/\Sigma Fe$ evolution for Kilauea also shows reduction as S degasses, similar to the melt inclusion measurements (Figure 9d). Thus, Sulfur_X appears to capture the degassing behavior recorded in Hawaiian melt inclusions.

5. IMPLICATIONS

5.1 General Application to Volcanic Systems

Our model results show that in Fuego magma, a typical H_2O-rich (4.5 wt.%) arc magma, with high initial $S^{6+}/\Sigma S$ (~0.7), ~70% of the sulfur in the melt is lost by degassing at pressures above 200 MPa (solid curves in Figure 8a). On the contrary, in Kilauea and Mauna Kea magmas, H_2O-poor (< 1wt.%) oceanic island basalts, with low initial $S^{6+}/\Sigma S$ (~0.1), almost no sulfur degasses until shallow pressures (<50 MPa, dashed curve in Figure 8a). The contrasting modeled sulfur degassing paths challenge the conventional view that sulfur only starts degassing at pressures lower than 150 MPa (e.g., Moore and Fabbi, 1971; Moore and Schilling, 1973; Webster et al., 2011). These models are still widely applied to interpret melt inclusion data and high-T volcanic gas data Instead, forward modeling by Sulfur_X shows that S degassing varies depending on the evolution of $kdS_{RxnI}^{v/m}$, $kdS_{RxnII}^{v/m}$, and $kdS_{RxnIa}^{v/m}$ as functions of temperature, pressure, fO_2, H_2O contents, and melt compositions, which affect each partition coefficient differently. For example, increasing fO_2 enhances $kdS_{RxnIa}^{v/m}$, decreases the $kdS_{RxnII}^{v/m}$ and does not affect $kdS_{RxnI}^{fl/m}$. Low H_2O in the system significantly suppresses RxnI and RxnIa, but it does not affect RxnII. Moreover, the combined partition coefficient also depends on S speciation in the melt and in the vapor (Equation 10). S degassing from reduced magmas with mostly S^{2-} in the melt would be dominated by $kdS_{RxnIa}^{fl/m}$or $kdS_{RxnI}^{v/m}$, depending on the SO_2/S_T in the vapor, whereas S degassing from oxidized magmas with mostly S^{6+} would be dictated by $kdS_{RxnII}^{v/m}$. At intermediate fO_2, both $kdS_{RxnII}^{v/m}$ and $kdS_{RxnIa}^{v/m}$ peak in the experimental data (Figure 3b), and both S^{2-} and S^{6+} exist in the melt (Figure 3a). This behavior is captured in Sulfur_X as well, as shown in Fig. 10. The combined effect of all three kds as a function of fO_2 leads to a peak in the combined kd at intermediate fO_2. High fO_2 causes $kdS_{RxnIa}^{v/m}$ to increase, but also causes the S^{2-} in the melt to decrease, thereby minimizing the contribution of $kdS_{RxnIa}^{v/m}$ to the $kdS_{combined}^{v/m}$. With decreasing fO_2, $kdS_{RxnII}^{v/m}$ increases but S^{6+} also decreases, thereby decreasing the contribution of $kdS_{RxnII}^{v/m}$ to the $kdS_{combined}^{v/m}$ (illustrated with the decrease in size of the purple dots in Fig 10). $kdS_{RxnI}^{v/m}$ shows no variation with fO_2 because O_2 is not involved in this reaction. And yet, as fO_2 increases, the amount of S^{2-} in the melt decreases, thereby decreasing the contribution of

$kdS^{v/m}_{RxnI}$ to the $kdS^{v/m}_{combined}$. While at low *fO₂*, $kdS^{v/m}_{RxnI}$ clearly dominates, and at high *fO₂*, $kdS^{v/m}_{RxnII}$ clearly dominates, all three reactions combine to create a maximum in $kdS^{v/m}_{combined}$ at intermediate *fO₂* (FMQ+1 in Fig. 10). This maximum leads to enhanced partitioning of S into the vapor, and thus more efficient degassing of S as observed for Fuego. This maximum in S partitioning to the vapor corresponds with the "minimum" in sulfur solubility in the melt described by Hughes et al. (submitted) in the simple S-O-silicate system (see also discussion of sulfur solubility "minimum" in O'Neill 2021).

It is important to also consider the effects of H_2O fugacity. At high H_2O fugacity, $kdS^{v/m}_{RxnI}$ is increased. Therefore, arc magmas like Fuego with intermediate fO_2 and high H_2O in the system can receive contributions from all three reactions to $kdS^{v/m}_{combined}$, and thus generally degas sulfur efficiently even at high pressures. In contrast, for relatively reduced and H_2O-poor ocean island basalts, the lack of S^{6+} minimizes the contribution from $kdS^{v/m}_{RxnII}$. At the same time, low fO_2 decreases $kdS^{v/m}_{RxnIa}$, and the low fH_2O decreases $kdS^{v/m}_{RxnI}$. Thus, partitioning of S to vapor is minimal, and only occurs significantly as *P* drops below 50 MPa, due to the –lnP effect on all kds.

S degassing could be even more complex than described above for Fuego and Hawaii. For example, reduced magma does not necessarily have high $kdS^{v/m}_{RxnIa}$ and low $kdS^{v/m}_{RxnII}$ if the calculated absolute fO_2 is not low, as shown in Kilauea melt inclusions and Mauna Kea submarine glasses. The absolute fO_2 is not only related to $Fe^{3+}/\Sigma Fe$ in the melt but also pressure, temperature, and melt composition (Kress and Carmichael, 1991). Dry magma may have low $kdS^{v/m}_{RxnI}$ and $kdS^{v/m}_{RxnIa}$ due to low water in the system, but $kdS^{v/m}_{RxnII}$ is not directly affected by H_2O and can still be significant, as shown in the case of Kilauea (Figure 9b). Therefore, if a dry system had more S^{6+} in the melt than magmas from Hawaii, a significant amount of S could still be degassed earlier than the Hawaiian cases. The general effects of initial H_2O and $S^{6+}/\Sigma S$ in the melt on sulfur degassing as a function of pressure are illustrated in Figure 10c. With high initial $S^{6+}/\Sigma S$ (~0.7) in the melt, significant sulfur degassing happens at pressures higher than 200 MPa, regardless of the H_2O contents, although higher H_2O contents result in slightly earlier degassing. On the contrary, with low initial $S^{6+}/\Sigma S$ (~0.1), S begins to degas deep only in wet magma (4.5 wt.% H_2O), similar to that in the magmas with high initial $S^{6+}/\Sigma S$. In this case, a decrease in H_2O concentration dramatically decreases S degassing depth. In addition, Sulfur_X shows that Fe and S redox can change in complex ways during decompression depending on the initial $S^{6+}/\Sigma S$ in the melt and other parameters. =Such feedbacks between S-Fe speciation in the melt, S speciation in the vapor and S degassing is captured for the first time by Sulfur_X.

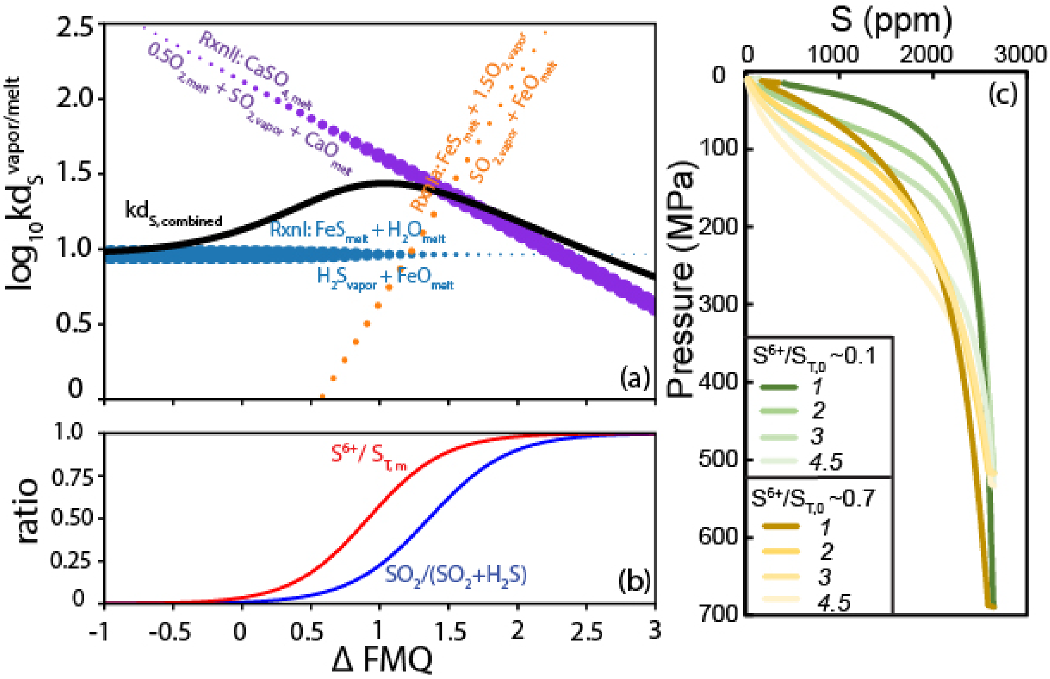

Figure 10. (a) Sulfur partition coefficients for RxnI (blue circles), RxnIa (orange circles), RxnII (purple circles), and combined sulfur partition coefficient (black curve) and (b) S speciation in the melt (red curve) and vapor (blue curve) as a function of oxygen fugacity (relative to FMQ buffer). (c) Modeled sulfur concentration for Fuego composition and 1030°C change as a function of pressure with low (0.1, green curves) and high (0.7, yellow curves) initial S^{6+}/S_T in

the melt. Under each condition, S degassing is modeled with different initial water contents (4.5, 3, 2, 1 wt.% H_2O). Other initial conditions are the same. In panel (a), the $kd_{S,combined}^{vapor/melt}$ is calculated using equation (7) in the text. The relative contribution of each reaction to $kd_{S,combined}^{vapor/melt}$ is indicated by the sizes of the symbols (as in equation 10). The kds are calculated at pressure of 300 MPa, temperature of 1030 °C, and melt composition of mafic Fuego melt inclusion.

5.2 Application to Volcanic Gas Compositions.

Sulfur_X also predicts the compositional evolution of co-existing vapor during magma decompression, which can be particularly useful in interpreting the CO_2/S_T molar ratio measured in high-T volcanic gases. First of all, CO_2/S_T ratios measured in high-T volcanic gases are often used to infer degassing depths in arc volcanic systems (Burton et al., 2007; Aiuppa et al., 2016; J. Maarten de Moor et al., 2016; Aiuppa et al., 2017)). For example, significant increase from 0.69-2.2 to a peak of 9 in CO_2/S_T ratio in volcanic gases from Villarrica and Turrialba volcanoes in the weeks before eruptions was interpreted as a surge of CO_2-enriched gas coming from ~30 MPa and 200-250 MPa for Villarrica and Turrialba, respectively (de Moor et al., 2016; Aiuppa et al., 2017) using the MP04 model (Moretti and Papale, 2004). In Figure 11, the predicted CO_2/S_T ratios in the co-existing vapor for Fuego are plotted against pressure. The predicted CO_2/S_T ratios between 0.5 and 10 agree well with the gas compositions collected at the surface from several Central American volcanoes (CAVA), and other arc volcanoes worldwide. For comparison, the CO_2/S_T ratios in the co-existing vapor for Fuego modeled by MP04 (Moretti and Papale, 2004), the most commonly used degassing model used by the volcanic gas community, are also plotted as a function of pressure in Figure 11. In contrast to orders of magnitudes increase in the predicted CO_2/S_T ratios from 0 to >200 MPa by MP04, Sulfur_X predicts that CO_2/S_T ratios for Fuego gases are < 5 at pressures lower than 300 MPa and only increase up to 10 at pressures above 500 MPa. Therefore, if the peak CO_2/S_T (~10) observed in high-*T* volcanic gases from arc volcanoes before eruptions truly represents a surge of a deep magma and gas, results from Sulfur_X for Fuego suggest that magma injection might happen much deeper than previously inferred (>500 MPa vs. ~10 MPa by MP04).

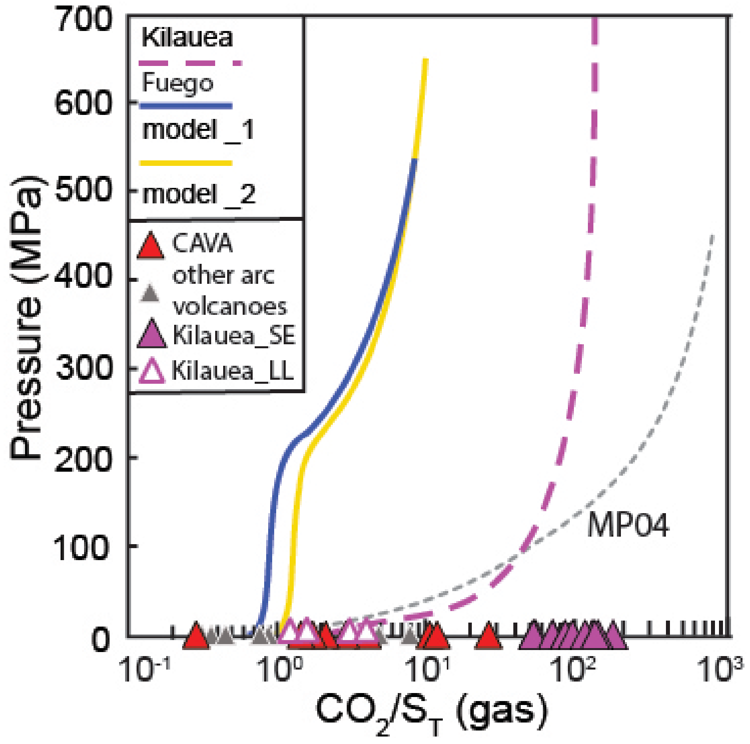

Figure 11. Modeled CO_2/S_T ratio in the co-existing vapor change as a function of pressure for Fuego and Kilauea. Modeled CO_2/S_T ratio in the co-existing vapor for Fuego by Moretti and Papale (2004) model (MP04), measured CO_2/S_T from some central American volcanoes (Aiuppa et al., 2014; Moussallam et al., 2017; Aiuppa et al., 2018), other arc volcanoes worldwide (Fischer, 2008), around Halemaumau lava lake in 1918-1919 (Kilauea_LL, Gerlach, 1980; Gerlach, 1986) and from Kilauea summit emissions from 1995 to 1999(Kilauea_SE, Gerlach et al., 2002)are also plotted for comparison.

In addition to being a depth signature, Aiuppa et al. (2014, 2017) proposed that the time-averaged CO_2/S_T ratio in volcanic gas can be a source feature, with some volcanoes having intrinsically higher ratios than others. Indeed, if the magma is completely degassed at 1 atm, Sulfur_X predicts that the CO_2/S_T molar ratio in the gas in equilibrium with the magma at 1 atm will be the same as the initial CO_2/S_T in the parental magma by closed-system degassing. For example, Figure 11 shows that the modeled CO_2/S_T ratio of gas emitted at 1 atm for Fuego is around 0.89 by model 1, and 1.35 by model 2. For Kilauea, in comparison, the value is 1.8. These numbers are very close to the initial molar ratio of the CO_2/S in the melt. However, Figure 11 also shows that CO_2/S_T ratios from passive degassing of most arc volcanoes are between 1 and 5, higher than the modeled CO_2/S_T ratio of gas emitted at 1 atm for Fuego. One possibility is that most arc volcanoes have higher CO_2/S than Fuego. The other possibility is that although collected at the surface, instead of equilibrating at 1 atm, the measured gas reflects an accumulation of gas derived from different depths, accounting for the variations of the measured CO_2/S in the volcanic gases. Last but not least, the predicted CO_2/S_T molar ratios for Kilauea volcano by Sulfur_X are about one order of magnitude higher than that for Fuego magma and remain greater than 50 along most of the decompression path, which results from little sulfur degassing at pressure higher than 50 MPa (see Fig. 8a). As pressure drops below 50 MPa, the predicted CO_2/S_T ratios for Kilauea volcano drops rapidly from 50 to ~1.8 at the surface. Gas compositions collected around Halemaumau lava lake in 1918-1919 (Gerlach, 1980; Gerlach, 1986) with CO_2/S_T molar ratios of 1.3-4.1 and directly measured from Kilauea summit emissions by 3 sets of summit correlation spectrometer (COSPEC) traverses from 1995 to 1999(Gerlach et al., 2002) with CO_2/S_T molar ratios between 50-200 are both plotted in Figure 11. Comparing the gas compositions to the modeled results suggests that gases collected around the Halemaumau lava lake released from pressures below 10 MPa from a parental magma enriched in CO_2 (type I magma in Gerlach, 1986) while the very high $CO2/S_T$ ratios from the 1995-1999 summit emissions suggests that the gases could have separated from the magma at pressures higher than 100 MPa.

6. **CONCLUSIONS**

1. Our analysis of existing sulfur partitioning experiments for basalt and basaltic andesite melts shows that sulfur degassing can be ascribed to three different reactions, S^{2-} in the melt degassing to H_2S in the vapor (RxnI), S^{2-} in the melt to SO_2 in the vapor (RxnIa), and S^{6+} in the melt to SO_2 in the vapor (RxnII). Guided by a broad set of experiments, Sulfur_X models S degassing from ascending magmas by calculating separate partition coefficients for each sulfur degassing reaction. This approach also allows Sulfur_X to account for pressure and temperature effects using thermodynamic rules instead of empirically extrapolating the results from low pressure experiments to high pressure (>200 MPa) where experiments are scarce. Sulfur_X then combines the three partition coefficients based on the sulfur species in the vapor and in the melt, which becomes the key parameter in Sulfur_X determining sulfur degassing, the combined sulfur partition coefficient. Sulfur_X also models the redox evolution of sulfur and iron in the system using redox budget conservation.
2. Applying Sulfur_X to Fuego, Kilauea and Mauna Kea shows that a typical wet (4.5 wt.% H_2O), oxidized arc magma with high initial $Fe^{3+}/\Sigma Fe$ and $S^{6+}/\Sigma S$ ratios can lose 2/3 of the sulfur in the melt by degassing at pressures above 200 MPa (eg. Fuego) whereas dry (< 1 wt.%) and more reduced oceanic island basalts with low initial $S^{6+}/\Sigma S$ ratios degas little sulfur until shallow pressures (<50 MPa, eg. Hawaii). Such pressure-sulfur degassing relationships presented by Sulfur_X bear directly on the interpretation of CO_2/S gas precursors to volcanic eruptions, of obvious relevancy to developing eruption forecasts.
3. For the first time, Sulfur _X explains the complex effects of fO_2 on sulfur degassing that is observed in experimental data. Sulfur_X predicts that the effect of all three kds and $S^{6+}/\Sigma S$ as

a function of fO_2 leads to a peak in the combined kd at intermediate fO_2, and so a maximum in sulfur degassing in arc magmas with high initial $S^{6+}/\Sigma S$ (>0.5) in the melt. Furthermore, comparison between the model results of the two case studies show the importance of H_2O concentration in the melt that increases both $kdS_{RxnI}^{fl/m}$ and $kdS_{RxnIa}^{fl/m}$, and H_2O fugacity that increases $kdS_{RxnI}^{fl/m}$. Both reactions are important in sulfur degassing in magmas dominated by S^{2-} in the melt.

4. Sulfur_X shows that the three sulfur degassing reactions (RxnI, RxnIa and RxnII), thus the process of sulfur degassing, are related to pressure, temperature, melt composition, H_2O fugacity, and oxygen fugacity of the system. Therefore, it calls to the importance of more melt inclusion studies with H_2O, S, reconstructed CO_2 concentration, more measurements on $Fe^{3+}/\Sigma Fe$ and $S^{6+}/\Sigma S$ ratios in the melt along degassing paths, and new experiments at pressures higher than 300 MPa with controlled P-T-fO_2 conditions .

ACKNOWLEDGEMENTS

We thank Sarah Shi and William Menke for help with the inverse iterative method; we thank Henry Towbin for suggestions on python coding. We acknowledge the support for SD from the National Science Foundation under Grant No. EAR-2017814.

Appendix A. Supplementary Material

Supplementary material associated with this manuscript includes a PDF file of detailed instructions for using Sulfur_X, a brief introduction to the Inverse Iterative Least Squares Method, supplementary figures and table.

Data Availability Statement

Python code of Sulfur_X and a CSV file of previous experimental data used for partition coefficients regression (Table. S2) can be accessed at: https://github.com/sdecho/Sulfur_X.git.

References

Aiuppa A., Bitetto M., Francofonte V., Velasquez G., Parra C. B., Giudice G., Liuzzo M., Moretti R., Moussallam Y., Peters N., Tamburello G., Valderrama O. A. and Curtis A. (2017) A CO 2 -gas precursor to the March 2015 Villarrica volcano eruption. *Geochemistry, Geophys. Geosystems* **18**, 2120–2132. Available at: http://doi.wiley.com/10.1002/2017GC006892.

Aiuppa A., Lo Coco E., Liuzzo M., Giudice G., Giuffrida G. and Moretti R. (2016) Terminal Strombolian activity at Etna's central craters during summer 2012: The most CO2-rich volcanic gas ever recorded at Mount Etna. *Geochem. J.* **50**, 123–138.

Aiuppa A., de Moor J. M., Arellano S., Coppola D., Francofonte V., Galle B., Giudice G., Liuzzo M., Mendoza E., Saballos A., Tamburello G., Battaglia A., Bitetto M., Gurrieri S., Laiolo M., Mastrolia A. and Moretti R. (2018) Tracking Formation of a Lava Lake From Ground and Space: Masaya Volcano (Nicaragua), 2014–2017. *Geochemistry, Geophys. Geosystems* **19**, 496–515.

Aiuppa A., Robidoux P., Tamburello G., Conde V., Galle B., Avard G., Bagnato E., De Moor J. M., Martínez M. and Muñóz A. (2014) Gas measurements from the Costa Rica-Nicaragua volcanic segment suggest possible along-arc variations in volcanic gas chemistry. *Earth Planet. Sci. Lett.* **407**, 134–147. Available at: http://dx.doi.org/10.1016/j.epsl.2014.09.041.

Anderson A. T. and Brown G. G. (1993) CO2 contents and formation pressures of some Kilauean melt inclusions. *Am. Mineral.* **78**, 794–803.

Aster E. M., Wallace P. J., Moore L. R., Watkins J., Gazel E. and Bodnar R. J. (2016) Reconstructing CO2 concentrations in basaltic melt inclusions using Raman analysis of vapor bubbles. *J. Volcanol. Geotherm. Res.* **323**, 148–162. Available at: http://dx.doi.org/10.1016/j.jvolgeores.2016.04.028.

Beermann O., Botcharnikov R. E., Holtz F., Diedrich O. and Nowak M. (2011) Temperature dependence of sulfide and sulfate solubility in olivine-saturated basaltic magmas. *Geochim. Cosmochim. Acta* **75**, 7612–7631. Available at: http://dx.doi.org/10.1016/j.gca.2011.09.024.

Beermann O., Botcharnikov R. E. and Nowak M. (2015) Partitioning of sulfur and chlorine between aqueous fluid and basaltic melt at 1050°C, 100 and 200 MPa. *Chem. Geol.* **418**, 132–157. Available at: http://dx.doi.org/10.1016/j.chemgeo.2015.08.008.

Binder B. and Keppler H. (2011) The oxidation state of sulfur in magmatic fluids. *Earth Planet. Sci. Lett.* **301**, 190–198.

Binder B., Wenzel T. and Keppler H. (2018) The partitioning of sulfur between multicomponent aqueous fluids and felsic melts. *Contrib. to Mineral. Petrol.*

Botcharnikov R. E., Linnen R. L., Wilke M., Holtz F., Jugo P. J. and Berndt J. (2011a) High gold concentrations in sulphide-bearing magma under oxidizing conditions. *Nat. Geosci.* **4**, 112–115.

Botcharnikov R. E., Linnen R. L., Wilke M., Holtz F., Jugo P. J. and Berndt J. (2011b) High gold concentrations in sulphide-bearing magma under oxidizing conditions. *Nat. Geosci.* **4**, 112–115. Available at: http://dx.doi.org/10.1038/ngeo1042.

Brounce M., Stolper E. and Eiler J. (2017) Redox variations in Mauna Kea lavas, the oxygen fugacity of the Hawaiian plume, and the role of volcanic gases in Earth's oxygenation. *Proc. Natl. Acad. Sci.* **114**, 8997–9002. Available at: http://www.pnas.org/lookup/doi/10.1073/pnas.1619527114.

Burgisser A., Alletti M. and Scaillet B. (2015) Simulating the behavior of volatiles belonging to the C-O-H-S system in silicate melts under magmatic conditions with the software D-Compress. *Comput. Geosci.* **79**, 1–14.

Burgisser A. and Scaillet B. (2007) Redox evolution of a degassing magma rising to the surface. *Nature* **445**, 194–7. Available at: http://www.ncbi.nlm.nih.gov/pubmed/17215841 [Accessed December 8, 2012].

Burton M., Allard P., Muré F. and La Spina A. (2007) Magmatic Gas Composition Reveals the Source Depth of Slug-Driven Strombolian Explosive Activity. *Science (80-.).* **317**, 227–230. Available at: https://www.science.org/doi/10.1126/science.1141900.

Danyushevsky L. V., Della-Pasqua F. N. and Sokolov S. (2000) Re-equilibration of melt inclusions trapped by magnesian olivine phenocrysts from subduction-related magmas: Petrological implications. *Contrib. to Mineral. Petrol.* **138**, 68–83.

Ding S., Dasgupta R. and Tsuno K. (2014) Sulfur concentration of martian basalts at sulfide saturation at high pressures and temperatures – Implications for deep sulfur cycle on Mars. *Geochim. Cosmochim. Acta* **131**, 227–246. Available at: http://www.sciencedirect.com/science/article/pii/S001670371400091X [Accessed March 26, 2014].

Esposito R., Klebesz R., Bartoli O., Klyukin Y. I., Moncada D., Doherty A. L. and Bodnar R. J. (2012) Application of the linkam TS1400XY heating stage to melt inclusion studies. *Cent. Eur. J. Geosci.* **4**, 208–218.

Evans K. A. (2006) Redox decoupling and redox budgets: Conceptual tools for the study of earth systems. *Geology* **34**, 489–492.

Fiege A., Behrens H., Holtz F. and Adams F. (2014a) Kinetic vs. thermodynamic control of degassing of H2O-S±Cl-bearing andesitic melts. *Geochim. Cosmochim. Acta* **125**, 241–264.

Fiege A., Holtz F., Behrens H., Mandeville C. W., Shimizu N., Crede L. S. and Göttlicher J. (2015) Experimental investigation of the S and S-isotope distribution between H2O–S±Cl fluids and basaltic melts during decompression. *Chem. Geol.* **393–394**, 36–54. Available at: http://dx.doi.org/10.1016/j.chemgeo.2014.11.012.

Fiege A., Holtz F., Shimizu N., Mandeville C. W., Behrens H. and Knipping J. L. (2014b) Sulfur isotope fractionation between fluid and andesitic melt: An experimental study. *Geochim. Cosmochim. Acta* **142**, 501–521.

Fischer T. P. (2008) Fluxes of volatiles (H2O, CO2, N2, Cl, F) from arc volcanoes. *Geochem. J.* **42**, 21–38. Available at: http://jlc.jst.go.jp/JST.JSTAGE/geochemj/42.21?from=Google [Accessed October 22, 2015].

Frost B. R. (1991) Chapter 1.INTRODUCTION TO OXYGEN FUGACITY AND ITS PETROLOGIC IMPORTANCE. In *Oxide Minerals* De Gruyter. pp. 1–10. Available at: https://www.degruyter.com/document/doi/10.1515/9781501508684-004/html.

Gaetani G. A., O'Leary J. A., Shimizu N., Bucholz C. E. and Newville M. (2012) Rapid reequilibration of H 2O and oxygen fugacity in olivine-hosted melt inclusions. *Geology* **40**, 915–918.

Gaetani G. A. and Watson E. B. (2000) Open system behavior of olivine-hosted melt inclusions. *Earth Planet. Sci. Lett.* **183**, 27–41.

Gaillard F. and Scaillet B. (2014) *A theoretical framework for volcanic degassing chemistry in a comparative planetology perspective and implications for planetary atmospheres*.,

Gaillard F., Scaillet B. and Arndt N. T. (2011) Atmospheric oxygenation caused by a change in volcanic degassing pressure. *Nature* **478**, 229–32. Available at:

http://www.ncbi.nlm.nih.gov/pubmed/21993759 [Accessed November 6, 2012].

Gennaro E., Paonita A., Iacono-Marziano G., Moussallam Y., Pichavant M., Peters N. and Martel C. (2020) Sulphur behaviour and redox conditions in etnean magmas during magma differentiation and degassing. *J. Petrol.* **61**.

Gerlach T. M. (1980) Evaluation of volcanic gas analyses from Kilauea volcano. *J. Volcanol. Geotherm. Res.* **7**, 295–317.

Gerlach T. M. (1986) Exsolution of H20 , CO2, and S during eruptive episodes. *J. Geophys. Res. Solid Earth* **91**, 12177–12185.

Gerlach T. M., McGee K. A., Elias T., Sutton A. J. and Doukas M. P. (2002) Carbon dioxide emission rate of Kīlauea Volcano: Implications for primary magma and the summit reservoir. *J. Geophys. Res. Solid Earth* **107**, ECV 3-1-ECV 3-15.

Hartley M. E., Maclennan J., Edmonds M. and Thordarson T. (2014) Reconstructing the deep CO 2 degassing behaviour of large basaltic fissure eruptions. *Earth Planet. Sci. Lett.* **393**, 120–131. Available at: http://dx.doi.org/10.1016/j.epsl.2014.02.031.

Haughton D. R., Roeder P. L. and Skinner B. J. (1974) Solubility of Sulfur in Mafic Magmas. *Econ. Geol.* **69**, 451–467. Available at: http://economicgeology.org/content/69/4/451.short [Accessed April 29, 2016].

Holloway J. R. (1987) Chapter 7. IGNEOUS FLUIDS. In *Thermodynamic Modeling of Geologic Materials* De Gruyter. pp. 211–234. Available at: https://www.degruyter.com/document/doi/10.1515/9781501508950-009/html.

Iacono-Marziano G., Morizet Y., Le Trong E. and Gaillard F. (2012) New experimental data and semi-empirical parameterization of H2O-CO2solubility in mafic melts. *Geochim. Cosmochim. Acta* **97**, 1–23. Available at: http://dx.doi.org/10.1016/j.gca.2012.08.035.

Johnson E. R., Wallace P. J., Cashman K. V. and Delgado Granados H. (2010) Degassing of volatiles (H2O, CO2, S, Cl) during ascent, crystallization, and eruption at mafic monogenetic volcanoes in central Mexico. *J. Volcanol. Geotherm. Res.* **197**, 225–238. Available at: https://linkinghub.elsevier.com/retrieve/pii/S0377027310000727.

Jugo P. J., Wilke M. and Botcharnikov R. E. (2010) Sulfur K-edge XANES analysis of natural and synthetic basaltic glasses: Implications for S speciation and S content as function of oxygen fugacity. *Geochim. Cosmochim. Acta* **74**, 5926–5938. Available at: http://linkinghub.elsevier.com/retrieve/pii/S0016703710004229 [Accessed May 24, 2013].

Kress V. C. and Carmichael I. S. E. (1991) The compressibility of silicate liquids containing Fe2O3 and the effect of composition, temperature, oxygen fugacity and pressure on their redox states. *Contrib. to Mineral. Petrol.* **108**, 82–92. Available at: http://link.springer.com/10.1007/BF00307328 [Accessed March 14, 2016].

Kress V., Greene L. E., Ortiz M. D. and Mioduszewski L. (2008) Thermochemistry of sulfide liquids IV: Density measurements and the thermodynamics of O-S-Fe-Ni-Cu liquids at low to moderate pressures. *Contrib. to Mineral. Petrol.* **156**, 785–797.

Lerner A. H., Wallace P. J., Shea T., Mourey A. J., Kelly P. J., Nadeau P. A., Elias T., Kern C., Clor L. E., Gansecki C., Lee R. L., Moore L. R. and Werner C. A. (2021) *The petrologic and degassing behavior of sulfur and other magmatic volatiles from the 2018 eruption of Kīlauea, Hawaiʻi: melt concentrations, magma storage depths, and magma recycling*., Springer Berlin Heidelberg. Available at: https://doi.org/10.1007/s00445-021-01459-y.

Lesne P., Kohn S. C., Blundy J., Witham F., Botcharnikov R. E. and Behrens H. (2011) Experimental Simulation of Closed-System Degassing in the System Basalt–H2O–CO2–S–Cl. *J. Petrol.* **52**, 1737–1762. Available at:

http://petrology.oxfordjournals.org/content/early/2011/08/04/petrology.egr027.short [Accessed October 22, 2015].

Liggins P., Shorttle O. and Rimmer P. B. (2020) Can volcanism build hydrogen-rich early atmospheres? *Earth Planet. Sci. Lett.* **550**, 116546. Available at: https://doi.org/10.1016/j.epsl.2020.116546.

Lloyd A. S., Plank T., Ruprecht P., Hauri E. H. and Rose W. (2013) Volatile loss from melt inclusions in pyroclasts of differing sizes. *Contrib. to Mineral. Petrol.* **165**, 129–153. Available at: http://link.springer.com/10.1007/s00410-012-0800-2.

Longpré M.-A., Stix J., Klügel A. and Shimizu N. (2017) Mantle to surface degassing of carbon- and sulphur-rich alkaline magma at El Hierro, Canary Islands. *Earth Planet. Sci. Lett.* **460**, 268–280. Available at: http://linkinghub.elsevier.com/retrieve/pii/S0012821X1630677X.

Masotta M., Keppler H. and Chaudhari A. (2016) Fluid-melt partitioning of sulfur in differentiated arc magmas and the sulfur yield of explosive volcanic eruptions. *Geochim. Cosmochim. Acta* **176**, 26–43. Available at: http://www.sciencedirect.com/science/article/pii/S0016703715007085 [Accessed February 16, 2016].

Matjuschkin V., Blundy J. D. and Brooker R. A. (2016) The effect of pressure on sulphur speciation in mid- to deep-crustal arc magmas and implications for the formation of porphyry copper deposits. *Contrib. to Mineral. Petrol.* **171**, 1–25.

Métrich N. and Wallace P. J. (2008) Volatile Abundances in Basaltic Magmas and Their Degassing Paths Tracked by Melt Inclusions. *Rev. Mineral. Geochemistry* **69**, 363–402.

Mironov N., Portnyagin M., Botcharnikov R., Gurenko A., Hoernle K. and Holtz F. (2015) Quantification of the CO2 budget and H2O–CO2 systematics in subduction-zone magmas through the experimental hydration of melt inclusions in olivine at high H2O pressure. *Earth Planet. Sci. Lett.* **425**, 1–11. Available at: http://dx.doi.org/10.1016/j.epsl.2015.05.043.

de Moor J. Maarten, Aiuppa A., Avard G., Wehrmann H., Dunbar N., Muller C., Tamburello G., Giudice G., Liuzzo M., Moretti R., Conde V. and Galle B. (2016) Turmoil at Turrialba Volcano (Costa Rica): Degassing and eruptive processes inferred from high-frequency gas monitoring. *J. Geophys. Res. Solid Earth* **121**, 5761–5775. Available at: http://doi.wiley.com/10.1002/2016JB013150.

de Moor J.M., Aiuppa A., Pacheco J., Avard G., Kern C., Liuzzo M., Martínez M., Giudice G. and Fischer T. P. (2016) Short-period volcanic gas precursors to phreatic eruptions: Insights from Poás Volcano, Costa Rica. *Earth Planet. Sci. Lett.* **442**, 218–227. Available at: http://dx.doi.org/10.1016/j.epsl.2016.02.056.

Moore J. G. and Fabbi B. P. (1971) An estimate of the juvenile sulfur content of basalt. *Contrib. to Mineral. Petrol.* **33**, 118–127.

Moore J. G. and Schilling J. G. (1973) Vesicles, water, and sulfur in Reykjanes Ridge basalts. *Contrib. to Mineral. Petrol.* **41**, 105–118.

Moore L. R., Gazel E., Tuohy R., Lloyd A. S., Esposito R., Steele-MacInnis M., Hauri E. H., Wallace P. J., Plank T. and Bodnar R. J. (2015) Bubbles matter: An assessment of the contribution of vapor bubbles to melt inclusion volatile budgets. *Am. Mineral.* **100**, 806–823. Available at: http://www.degruyter.com/dg/viewarticle.fullcontentlink:pdfeventlink/$002fj$002fammin.2015.100.issue-4$002fam-2015-5036$002fam-2015-5036.pdf/am-2015-5036.pdf?t:ac=j$002fammin.2015.100.issue-4$002fam-2015-5036$002fam-2015-5036.xml

[Accessed November 1, 2016].

Moore L. R., Mironov N., Portnyagin M., Gazel E. and Bodnar R. J. (2018) Volatile contents of primitive bubble-bearing melt inclusions from Klyuchevskoy volcano, Kamchatka: Comparison of volatile contents determined by mass-balance versus experimental homogenization. *J. Volcanol. Geotherm. Res.* **358**, 124–131. Available at: https://doi.org/10.1016/j.jvolgeores.2018.03.007.

Moretti R. and Papale P. (2004) On the oxidation state and volatile behavior in multicomponent gas–melt equilibria. *Chem. Geol.* **213**, 265–280. Available at: https://linkinghub.elsevier.com/retrieve/pii/S0009254104003468.

Moune S., Holtz F. and Botcharnikov R. E. (2008) Sulphur solubility in andesitic to basaltic melts: implications for Hekla volcano. *Contrib. to Mineral. Petrol.* **157**, 691–707. Available at: http://www.springerlink.com/index/10.1007/s00410-008-0359-0 [Accessed May 25, 2012].

Moussallam Y., Edmonds M., Scaillet B., Peters N., Gennaro E., Sides I. and Oppenheimer C. (2016) The impact of degassing on the oxidation state of basaltic magmas: A case study of Kīlauea volcano. *Earth Planet. Sci. Lett.* **450**, 317–325. Available at: http://dx.doi.org/10.1016/j.epsl.2016.06.031.

Moussallam Y., Tamburello G., Peters N., Apaza F., Schipper C. I., Curtis A., Aiuppa A., Masias P., Boichu M., Bauduin S., Barnie T., Bani P., Giudice G. and Moussallam M. (2017) Volcanic gas emissions and degassing dynamics at Ubinas and Sabancaya volcanoes; implications for the volatile budget of the central volcanic zone. *J. Volcanol. Geotherm. Res.* **343**, 181–191. Available at: http://dx.doi.org/10.1016/j.jvolgeores.2017.06.027.

Muth M. J. and Wallace P. J. (2021) Slab-derived sulfate generates oxidized basaltic magmas in the southern Cascade arc (California, USA). *Geology* **49**, 1177–1181.

Nash W. M., Smythe D. J. and Wood B. J. (2019) Compositional and temperature effects on sulfur speciation and solubility in silicate melts. *Earth Planet. Sci. Lett.* **507**, 187–198. Available at: https://doi.org/10.1016/j.epsl.2018.12.006.

Newman S. and Lowenstern J. B. (2002) Volatile Calc : a silicate melt – H2O – CO2 solution model written in Visual Basic for excel. *Comput. Geosci.* **28**, 597–604.

O'Neill H. S. C. (2021) Comment on "Compositional and temperature effects on sulfur speciation and solubility in silicate melts" by Nash et al. [Earth Planet. Sci. Lett. 507 (2019) 187–198]. *Earth Planet. Sci. Lett.* **560**, 116843. Available at: https://doi.org/10.1016/j.epsl.2021.116843.

O'Neill H. S. C. and Eggins S. M. (2002) The effect of melt composition on trace element partitioning: An experimental investigation of the activity coefficients of FeO, NiO, CoO, MoO2 and MoO3 in silicate melts. *Chem. Geol.* **186**, 151–181.

O'Neill H. S. C. and Mavrogenes J. A. (2002) The Sulfide Capacity and the Sulfur Content at Sulfide Saturation of Silicate Melts at 1400°C and 1 bar. *J. Petrol.* **43**, 1049–1087.

Pingfang Shi and Saxena S. K. (1992) Thermodynamic modeling of the C-H-O-S fluid system. *Am. Mineral.* **77**, 1038–1049.

Rasmussen D. J., Kyle P. R., Wallace P. J., Sims K. W. W., Gaetani G. A. and Phillips E. H. (2017) Understanding Degassing and Transport of CO2-rich Alkalic Magmas at Ross Island, Antarctica using Olivine-Hosted Melt Inclusions. *J. Petrol.* **58**, 841–862.

Rasmussen D. J., Plank T. A., Wallace P. J., Newcombe M. E. and Lowenstern J. B. (2020) Vapor-bubble growth in olivine-hosted melt inclusions. *Am. Mineral.* **105**, 1898–1919.

Righter K., Pando K. and Danielson L. R. (2009) Experimental evidence for sulfur-rich martian magmas: Implications for volcanism and surficial sulfur sources. *Earth Planet. Sci. Lett.* **288**, 235–243. Available at: http://linkinghub.elsevier.com/retrieve/pii/S0012821X09005615 [Accessed May 24, 2013].

Rose W. I., Anderson A. T., Woodruff L. G. and Bonis S. B. (1978) The October 1974 basaltic tephra from Fuego volcano: Description and history of the magma body. *J. Volcanol. Geotherm. Res.* **4**, 3–53.

Scaillet B. and Macdonald R. A. Y. (2003) Experimental Constraints on the Relationships between Peralkaline Rhyolites of the Kenya Rift Valley. **44**.

Scaillet B. and Pichavant M. (2003) Experimental constraints on volatile abundances in arc magmas and their implications for degassing processes. *Geol. Soc. London, Spec. Publ.* **213**, 23–52. Available at: http://sp.lyellcollection.org/content/213/1/23.short [Accessed December 29, 2012].

Sisson T. W. and Layne G. D. (1993) H2O in basalt and basaltic andesite glass inclusions from four subduction-related volcanoes. *Earth Planet. Sci. Lett.* **117**, 619–635. Available at: https://linkinghub.elsevier.com/retrieve/pii/0012821X9390107K.

Steele-Macinnis M., Esposito R. and Bodnar R. J. (2011) Thermodynamic Model for the Effect of Post-entrapment Crystallization on the H2O-CO2 Systematics of Vapor-saturated, Silicate Melt Inclusions. *J. Petrol.* **52**, 2461–2482. Available at: https://academic.oup.com/petrology/article-lookup/doi/10.1093/petrology/egr052.

Steele-MacInnis M., Esposito R., Moore L. R. and Hartley M. E. (2017) Heterogeneously entrapped, vapor-rich melt inclusions record pre-eruptive magmatic volatile contents. *Contrib. to Mineral. Petrol.* **172**, 18. Available at: http://link.springer.com/10.1007/s00410-017-1343-3.

Stolper E. and Holloway J. R. (1988) Experimental determination of the solubility of carbon dioxide in molten basalt at low pressure. *Earth Planet. Sci. Lett.* **87**, 397–408.

Tuohy R. M., Wallace P. J., Loewen M. W., Swanson D. A. and Kent A. J. R. (2016) Magma transport and olivine crystallization depths in Kīlauea’s east rift zone inferred from experimentally rehomogenized melt inclusions. *Geochim. Cosmochim. Acta* **185**, 232–250. Available at: http://dx.doi.org/10.1016/j.gca.2016.04.020.

Wallace P. J., Kamenetsky V. S. and Cervantes P. (2015) Melt inclusion CO2 contents, pressures of olivine crystallization, and the problem of shrinkage bubbles. *Am. Mineral.* **100**, 787–794. Available at: http://www.degruyter.com/dg/viewarticle.fullcontentlink:pdfeventlink/$002fj$002fammin.2015.100.issue-4$002fam-2015-5029$002fam-2015-5029.pdf/am-2015-5029.pdf?t:ac=j$002fammin.2015.100.issue-4$002fam-2015-5029$002fam-2015-5029.xml [Accessed November 1, 2016].

Webster J. D. and Botcharnikov R. E. (2011) Distribution of Sulfur Between Melt and Fluid in S-O-H-C-Cl-Bearing Magmatic Systems at Shallow Crustal Pressures and Temperatures. *Rev. Mineral. Geochemistry* **73**, 247–283. Available at: http://rimg.geoscienceworld.org/cgi/doi/10.2138/rmg.2011.73.9 [Accessed March 17, 2012].

Webster J. D., Goldoff B. and Shimizu N. (2011) C-O-H-S fluids and granitic magma: How S partitions and modifies CO2 concentrations of fluid-saturated felsic melt at 200 MPa. *Contrib. to Mineral. Petrol.* **162**, 849–865.

Werner C., Fischer T. P., Aiuppa A., Edmonds M., Cardellini C., Carn S., Chiodini G., Cottrell E., Burton M., Shinohara H. and Allard P. (2019) Carbon Dioxide Emissions from

Subaerial Volcanic Regions. In *Deep Carbon* Cambridge University Press. pp. 188–236. Available at: https://www.cambridge.org/core/product/identifier/9781108677950%23CN-bp-8/type/book_part.

Werner C., Rasmussen D. J., Plank T., Kelly P. J., Kern C., Lopez T., Gliss J., Power J. A., Roman D. C., Izbekov P. and Lyons J. (2020) Linking Subsurface to Surface Using Gas Emission and Melt Inclusion Data at Mount Cleveland Volcano, Alaska. *Geochemistry, Geophys. Geosystems* **21**, 1–33.

Wilke M., Klimm K. and Kohn S. C. (2011) Spectroscopic Studies on Sulfur Speciation in Synthetic and Natural Glasses. *Rev. Mineral. Geochemistry* **73**, 41–78. Available at: http://rimg.geoscienceworld.org/cgi/doi/10.2138/rmg.2011.73.3 [Accessed April 19, 2012].

Witham F., Blundy J., Kohn S. C., Lesne P., Dixon J., Churakov S. V. and Botcharnikov R. (2012) SolEx: A model for mixed COHSCl-volatile solubilities and exsolved gas compositions in basalt. *Comput. Geosci.* **45**, 87–97. Available at: http://www.sciencedirect.com/science/article/pii/S0098300411003554 [Accessed October 23, 2015].

Wood B. J., Nash W. M. and Smythe D. J. (2021) Reply to: O'Neill, H.S., 2021: "Comment on 'Compositional and temperature effects on sulfur speciation and solubility in silicate melts' " by Nash et al. [Earth Planet. Sci. Lett. 507 (2019) 187–198]. *Earth Planet. Sci. Lett.* **560**, 116769. Available at: https://doi.org/10.1016/j.epsl.2021.116769.

Zajacz Z. (2014) The effect of melt composition on the partitioning of oxidized sulfur between silicate melts and magmatic volatiles. *Geochim. Cosmochim. Acta* **158**, 223–244.

Zajacz Z., Candela P. A., Piccoli P. M. and Sanchez-Valle C. (2012) The partitioning of sulfur and chlorine between andesite melts and magmatic volatiles and the exchange coefficients of major cations. *Geochim. Cosmochim. Acta* **89**, 81–101. Available at: https://linkinghub.elsevier.com/retrieve/pii/S001670371200244X.

Zajacz Z., Candela P. A., Piccoli P. M., Sanchez-Valle C. and Wälle M. (2013) Solubility and partitioning behavior of Au, Cu, Ag and reduced S in magmas. *Geochim. Cosmochim. Acta* **112**, 288–304.